

Optimizing Entanglement Distribution Protocols: Maximizing Classical Information in Quantum Networks

Ethan Sanchez Hidalgo*, Diego Zafra Bono, Guillermo Encinas Lago, J. Xavier Salvat Lozano*, Jose A. Ayala-Romero, Xavier Costa Perez, *Senior Member, IEEE*

Abstract—Efficient entanglement distribution is the foundational challenge in realizing large-scale Quantum Networks (QNs). However, state-of-the-art solutions are frequently limited by restrictive operational assumptions, prohibitive computational complexities, and performance metrics that misalign with practical application needs. To overcome these barriers, this paper addresses the entanglement distribution problem by introducing four pivotal advances. First, recognizing that the primary application of quantum communication is the transmission of private information, we derive the *Ensemble Capacity (EC)*, a novel metric that explicitly quantifies the secure classical information enabled by the entanglement distribution. Second, we propose a generalized mathematical formulation that removes legacy structural restrictions in the solution space. Our formulation supports an unconstrained, arbitrary sequencing of entanglement swapping and purification. Third, to efficiently navigate the resulting combinatorial optimization space, we introduce a novel Dynamic Programming (DP)-based hypergraph generation algorithm. Unlike prior methods, our approach avoids artificial fidelity quantization, preserving exact, continuous fidelities while proactively pruning sub-optimal trajectories. Finally, we encapsulate these algorithmic solutions into *CODE*, a system-level, two-tiered orchestration framework designed to enable near-real-time network responsiveness. Extensive evaluations confirm that our DP-driven architecture yields superior private classical information capacity and significant reductions in computational complexity, successfully meeting the strict sub-second latency thresholds required for dynamic QN operation.

Index Terms—Quantum Network, Entanglement Distribution, Optimal Resource Allocation

I. INTRODUCTION

Quantum Networks are the next step in secure communications, as they leverage the principles of quantum physics to securely transmit data using entangled particles—typically polarized photons of light transmitted through optical fibers. QNs enable the development of new applications such as Quantum Key Distribution (QKD) [1], Quantum Secret Sharing (QSS) [2] or Quantum Secure Direct Communication (QSDC) [3]. These applications rely on the efficient generation

*Corresponding authors.

Ethan Sanchez Hidalgo and Diego Zafra Bono were with i2CAT Foundation, Barcelona, Spain (email: ethan.sanchez.hidalgo@gmail.com, diegozafraono@gmail.com). Guillermo Encinas Lago is with i2CAT Foundation, Barcelona, Spain (e-mail: guillermo.encinas@i2cat.net). J. Xavier Salvat Lozano is with NEC Laboratories Europe GmbH, Heidelberg, Germany and Universitat Autònoma de Barcelona (UAB), Bellaterra, Spain (e-mail: josep.xavier.salvat@neclab.eu). Jose A. Ayala-Romero is with NEC Laboratories Europe GmbH, Heidelberg, Germany (e-mail: jose.ayala@neclab.eu). Xavier Costa-Pérez is with NEC Laboratories Europe GmbH, Heidelberg, Germany, i2CAT Foundation and ICREA, Barcelona, Spain (e-mail: xavier.costa@ieee.org).

Work supported by the European Commission through grants No. 101139270 (ORIGAMI) and SNS-JU-101192521 (Multi-X) and by the CERCA Programme.

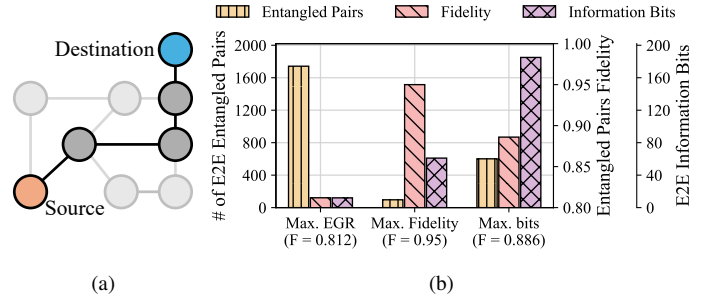


Fig. 1: Performance analysis of the proposed quantum network. (a) Schematic representation. (b) Comparison of different entanglement distribution strategies.

and distribution of Entangled Pairs (EPs) across distant nodes to create and sustain reliable and private end-to-end communication links. However, distributing EPs across long distances is far from trivial. Optical fiber losses grow exponentially with distance [4], and unlike classical signals, quantum states cannot simply be amplified or regenerated as a consequence of the no-cloning theorem [5]. These constraints pose strict fundamental limits on direct data transmission over QNs, highlighting the need for specialized solutions.

Quantum repeaters [6], [7] perform entanglement swapping [8], connecting shorter entangled segments to establish entanglement over longer distances. Because repeater operations are imperfect, the *fidelity* the measure of an EP's proximity to its ideal reference state rapidly deteriorates. To address this, repeaters perform entanglement purification [9], combining multiple low-fidelity pairs to distill fewer high-fidelity pairs. Swapping and purification operations are inherently interdependent: swapping extends communication range but degrades fidelity, while purification increases fidelity at the cost of reducing the number of available EPs. As a result, QN performance depends heavily on link management strategies that determine which repeaters (and in what order) execute these operations to optimize end-to-end communication [10]–[12]. In this work, we address the *Entanglement Distribution Problem*: the generation, transmission, and management of Entangled Pairs across a Quantum Network.

A fundamental limitation of current entanglement distribution literature is its prevailing focus on maximizing the raw Entanglement Generation Rate (EGR) subject to hard fidelity constraints. Optimizing raw generation rates does not intrinsically translate to the maximization of actual data transmission. Specifically, it fails to capture the *classical private information* capacity, which quantifies the volume of data that can be reliably transmitted over a quantum channel [13]. To

address this, we shift the optimization objective entirely. We introduce classical private information as the primary objective and derive a novel performance metric—the Ensemble Capacity (EC) (see Sec. IV)—which rigorously quantifies the actual secure classical bit rate enabled by distributed entanglement.

Figure 1 demonstrates the critical flaw in rate- or fidelity-centric optimization using a 4-hop network topology. For simplicity, all links are assumed to have identical distance (70 km), generation budget (2760 Entangled pairs per second), and initial fidelity. A common approach in the literature is the maximization of the end-to-end EGR (*Max. EGR*) [11], [14]–[17]. While this method achieves high pair volume, the resulting end-to-end fidelity is frequently compromised, severely restricting the transmission of private information. Conversely, the *Max. Fidelity* approach, as in [18], [19], starves the network (EGR reduced by a factor of 17x), but ensures a significantly higher state accuracy, enabling the transmission of nearly 5x the number of private bits compared to the previous approach. Finally, by directly optimizing the EC (*Max. bits*), our strategy strikes the optimal balance between rate and fidelity, achieving a 3x improvement in secure information bits over standard approaches. To the best of our knowledge, this work is the first to consider this dimension in the entanglement distribution problem.

Optimizing the Ensemble Capacity necessitates a fully generalized solution space that permits arbitrary sequencing of swapping and purification operations. Artificially forcing purification to occur strictly before swapping [20]–[22] leaves significant performance potential untapped. While unconstrained sequencing has been previously attempted using hypergraphs [14], these models relied on the strict discretization of continuous fidelity values to maintain computational feasibility, leading to inherent degraded state accuracy and sub-optimal operational decisions that compromise the end-to-end entanglement distribution performance. To overcome these limitations, we introduce a Dynamic Programming (DP)-based hypergraph generation mechanism (Sec. VI-B). This methodology provides two pivotal advantages. First, it preserves the exact, continuous fidelity of the distributed EPs, bypassing the deleterious effects of artificial quantization. Second, the algorithm guarantees a finite and tractable solution space by identifying and pruning low-performing operational sequences in advance. As validated by our evaluation, this DP-driven approach achieves a significant reduction in computational complexity with almost negligible accuracy loss, yielding superior end-to-end performance compared to prior art.

However, even an efficient hypergraph generation algorithm remains computationally heavy for the real-time-scale dynamics of a physical Quantum Network. To bridge the gap between theoretical optimization and practical deployment, we introduce a comprehensive system-level orchestration framework termed CODE (Sec. VI-E), divided into two nested operational loops. The *Outer Loop* comprises the computationally intensive processing steps and operates on a coarse timescale (seconds to minutes), monitoring the network conditions and demands. Conversely, the *Inner Loop* operates on a finer timescale (10ms to 1s), leveraging the pre-computed structures to handle rapid fluctuations in user

demand and dynamically allocate resources in near-real-time. Our evaluations confirm that, unlike existing benchmarks, our hierarchical design satisfies the stringent latency constraints imperative for near-real-time QN operation. To the best of our knowledge, CODE provides the first system-level architecture designed to solve the Entanglement Distribution Problem for practical deployment.

We summarize the contributions of this work as follows:

- 1) **Ensemble Capacity Metric:** We derive the Ensemble Capacity to directly quantify the volume of private classical information transmissible over a quantum channel. This shifts the fundamental optimization objective from raw generation rates to actual secure data throughput.
- 2) **Generalized Operational Sequencing:** We formulate a fully unconstrained mathematical model for entanglement distribution. By lifting restrictive structural constraints to accommodate the arbitrary sequencing of swapping and purification operations, our model unlocks previously unreachable regions of the optimization space.
- 3) **Continuous-Fidelity DP Hypergraphs:** We introduce a Dynamic Programming-based hypergraph generation algorithm to tractably navigate this vast combinatorial space. By preserving exact continuous fidelities and systematically pruning low-performing branches, we completely eliminate the accuracy degradation inherent in artificial state discretization.
- 4) **System-Level Orchestration Framework:** We encapsulate our algorithmic solution into a practical, dual-loop network architecture. Rigorous benchmarking confirms that by decoupling heavy background optimization from near-real-time execution, our framework successfully meets the strict latency constraints required to manage real-world quantum networks.

II. RELATED WORK

Previous research on entanglement distribution has mainly focused on two different directions. On the one hand, many studies aim to maximize the end-to-end EGR without purification operations, which results in poor end-to-end fidelity, often using EGR-based routing metrics to select paths [11], [15]–[17]. On the other hand, other works set a minimum end-to-end fidelity constraint to compute the best paths [12], [23], [24] but neglect purification. More recently, several works incorporated purification into path selection. The works [20]–[22] developed different strategies to ensure a minimum per-link fidelity through purification before swapping. [25] formulates a joint routing/purification problem and designs algorithms for fidelity-guaranteed paths. In contrast, this work incorporates both entanglement swapping and purification operations. Critically, unlike prior studies that restrict purification to the initial step, our formulation allows purification to be applied at any stage of the operational sequence. By removing these constraints on the sequence of operations, our approach enables exploration of the full performance potential of QNs.

More recently, the work more closely related to ours [14] considers both purification and swapping without constraints in the sequence of operations. This study aims to maximize

the EGR under fidelity constraints. Nevertheless, the maximization of the EGR does not necessarily correspond to the maximization of information transmission or *classical private information*, which quantifies how much private information can be securely transmitted over a quantum channel [13]. In contrast to previous works, we consider the classical private information maximization as the main objective, as it directly quantifies the communication capabilities of the network. For that purpose, we derive a novel performance metric (Ensemble Capacity, see Sec. IV) that quantifies the private classical bits of communication enabled by shared entanglement.

Classical private information has also been studied analytically to bound secure key rates [26], [27]. These works provide theoretical limits derived from simplified models of the networks, which are not practical for developing or optimizing entanglement distribution protocols. The work in [10] is the first to optimize entanglement routing using distillable entanglement, related to classical private information. However, it is limited to symmetric topologies, short paths, and shallow purification, providing a narrow perspective on the problem.

III. BACKGROUND

Quantum communication in quantum networks builds upon the following key principles:

1) *Quantum entanglement*: Entanglement [28] is a phenomenon in quantum mechanics in which two or more particles share a global state that cannot be described by their local states. Measurements on one particle instantaneously correlate with outcomes on its entangled counterpart, a feature known as *quantum non-locality*. Entangled pairs are the primary resource in QNs, which generate, maintain, and distribute them across spatially separated nodes. The quality of an Entangled Pair is quantified by the *fidelity* F , measuring the overlap between the actual state ρ and a target Bell state $|\Phi^+\rangle$:

$$F := \langle \Phi^+ | \rho | \Phi^+ \rangle, \quad (1)$$

where $F = 1$ indicates a perfectly entangled pair, and values near 0 indicate near orthogonality. State-of-the-art techniques to generate entangled pairs include semiconductor quantum dots [29], nitrogen-vacancy centers in diamond [30], atomic ensembles [31], and nonlinear optical methods such as Spontaneous Parametric Down Conversion [32].

2) *Quantum teleportation and Entanglement swapping*: Quantum teleportation [33] is the fundamental mechanism for transferring a quantum state between distant parties without physical transmission, strictly respecting the no-cloning theorem [5]. Operating within the Local Operations and Classical Communication (LOCC) framework, it requires a pre-shared Entangled Pair. The sender performs a joint Bell-state measurement (BSM) on the target qubit and their half of the entangled pair. Upon receiving the two-bit classical measurement outcome from the sender, the receiver applies a conditional unitary operation to reconstruct the original state.

Entanglement swapping [8] leverages this exact mechanism to establish long-distance communication by effectively teleporting entanglement itself. Given two independent pairs, (A, B) and (C, D) , an intermediate node holding particles

B and C performs a local BSM on them. Once the intermediate node relays the classical measurement outcome to the remote end nodes for local corrections, particles A and D become entangled despite never physically interacting, seamlessly bridging the two initial segments.

3) *Entanglement purification*: Entanglement purification or distillation [34], is a probabilistic process designed to enhance the fidelity of EPs. Purification extracts a smaller set of entangled pairs with higher fidelity from a large set of noisy or imperfectly entangled pairs [35].

IV. ENSEMBLE CAPACITY: CLASSICAL PRIVATE INFORMATION ANALYSIS

In this section, we introduce a novel metric to evaluate the performance of a QN: the Ensemble Capacity. While metrics such as the end-to-end fidelity of shared pairs [12], the end-to-end Entanglement Generation Rate (EGR) [11], the request fulfillment rate [36], and qubit utilization rate [37] provide valuable insights, they do not directly quantify the network's data transmission capabilities. In contrast, Ensemble Capacity measures the volume of private classical information bits that two end parties can securely exchange. This metric inherently captures the trade-off between the quantity of shared entangled pairs (i.e. where the aggregate count is directly proportional to the EGR) and their fidelity. To address the entanglement distribution problem from a capacity-centric perspective (see Sec. V) we first define the capacity of a single Entangled Pair (see Sec. IV-A) and then generalize this definition to a set of entangled pairs, formally defining the Ensemble Capacity (see Sec. IV-B). Finally, we discuss the universality of this metric, making the Ensemble Capacity applicable across diverse quantum applications (Sec. IV-C).

A. Single Entangled Pair Capacity

We define the capacity \mathcal{C} of a single Entangled Pair ρ shared between a source s and destination d nodes as the amount of private classical bits $\mathcal{C}(\rho)$ that can be securely transmitted from s to d using ρ assisted by adaptive Local Operations and Classical Communication (LOCC) operations.

Let F denote the fidelity of an EP ρ modeled as a mixed two-qubit state (i.e., a Werner state modeling imperfect entanglement as a combination of a Bell state and white noise [38]). As established in [39], teleportation over noisy entangled states, is equivalent to transmitting through a depolarizing quantum channel \mathcal{E}_p of parameter $p = \frac{4(1-F)}{3}$, i.e. $\mathcal{C}(\rho) = \mathcal{C}(\mathcal{E}_p)$. Consequently, the capacity $\mathcal{C}(\rho)$ is bounded by

$$k(p) - \frac{3p}{4} \log_2(3) \leq \mathcal{C}(\rho) \leq k(p), \quad (2)$$

where $k(p) := 1 - H_2(3p/4)$, and H_2 is the binary Shannon entropy. These bounds are derived assuming arbitrary teleportation protocols; this generality holds because QKD-style protocols can be reformulated in terms of entanglement-based teleportation, as shown in [40].

B. Multiple Entangled Pairs Capacity

Transmitting information via a single pair alone is often inefficient. Instead, entanglement is typically generated in a parallel, producing multiple end-to-end pairs simultaneously. Therefore, we generalize the single-pair capacity to a network-level figure of merit: the *Ensemble Capacity*. We define an ensemble as a set of Entangled Pairs $\{\rho_i\}_{i=1}^n$ shared between a source s and destination d . The Ensemble Capacity (EC), denoted by $\mathcal{C}(\otimes_{i=1}^n \rho_i)$, is the number of private classical bits that can be securely transmitted between s and d by using the ensemble $\{\rho_i\}_{i=1}^n$ and adaptive LOCC operations.

While this definition captures the theoretical maximum data-carrying potential, computing $\mathcal{C}(\otimes \rho_i)$ is generally intractable due to the complexity of evaluating collective operations over entangled resources. Consequently, following the fundamental bounds in [4], we adopt a conservative approximation by considering a *lower bound* on this quantity as the sum of individual pair capacities, $\sum_{i=1}^n \mathcal{C}(\rho_i)$.

By substituting $p = \frac{4(1-F)}{3}$ into the lower bound of Eq. (2), we obtain the computable lower bound for the Ensemble Capacity:

$$\mathcal{C}(\otimes_{i=1}^n \rho_i) = \sum_{i=1}^n k \left(\frac{4(1-F_i)}{3} \right) - (1-F_i) \log_2(3). \quad (3)$$

C. Ensemble Capacity as a Universal Metric

The goal of quantum networks—regardless of the specific application—is always to maximize the number of shared high-fidelity entangled pairs in the least amount of time. However, the definition of “high-fidelity” varies across use cases. For example, QKD requires a minimum threshold of approximately $F \geq 0.8$ [41], whereas distributed quantum computing typically demands fidelity exceeding 0.9 [42], [43]. This difference exposes a key limitation of the prevailing optimization methodology, which typically maximizes the entanglement generation rate subject to a hard fidelity constraint [12], [21], [25]. Choosing a fixed threshold hard-codes the target application into the network design, yielding solutions that are not comparable across use cases and collapsing the subtle pair quantity and fidelity trade-off into an arbitrary operating point. In contrast, Ensemble Capacity provides a use-case-agnostic objective. It characterizes the aggregate end-to-end entanglement the network can deliver across all quality levels, allowing the network to be optimized once for maximal provisioning capability while enabling specific applications to select their own operating regions.

V. ENTANGLEMENT DISTRIBUTION PROBLEM FORMULATION

In this section, we present a mathematical framework for the Entanglement Distribution Problem that maximizes the Ensemble Capacity between a source s and a destination d by optimizing the underlying sequences of purification and swapping operations. Our formulation introduces three fundamental advancements over existing literature. First, it generalizes the selection of a single sequence of operations

along a path P . Instead, our formulation allows multiple sequences to execute concurrently along the same path, generating an ensemble of distinguishable end-to-end EPs [10], [22]. Second, it allows purification operations at any hop of the distribution sequence. This flexibility significantly expands the solution space, unlocking high-fidelity strategies that are inaccessible to simpler models [20], [21]. Third, our formulation enables dynamic resource pooling across multiple, potentially overlapping paths. By jointly optimizing over non-disjoint paths, the model recognizes when entangled pairs on shared links are underutilized due to bottlenecks elsewhere in the network. Consequently, our approach reallocates these residual resources to co-existing operational sequences, ensuring that no entanglement is wasted when chaining operations across the infrastructure [16], [23].

A. Network Model and Notation

A Quantum Network is mathematically modeled as a graph $G = (V, E)$, where the vertex set V represents the quantum repeaters and the edge set E represents the physical links connecting adjacent nodes. Each edge $e \in E$ is characterized by the tuple (u, v, r_e, f_e) , where u and v are two physically adjacent nodes, r_e denotes the mean entanglement generation rate (in Hz) and f_e represents the mean fidelity of the entangled pairs generated over the fiber-optic channel. We define the accumulation window T_w as the time interval during which entangled pairs are accumulated in quantum memories. We assume T_w is bounded by the quantum memory coherence time (see Sec. VII-C3). Let $\mathcal{P}_{s,d}$ be the set of all simple paths between source s and destination d , where each path $P \in \mathcal{P}_{s,d}$ is an ordered sequence of adjacent physical links.

B. Sequences of operations

To establish an end-to-end entangled link between a source s and a destination d over a path P , P must be transformed into a single virtual link through a structured sequence of entanglement swapping and purification operations. Establishing end-to-end connectivity for a path of length k requires exactly $k - 1$ swaps and provides $2(k - 1) + 1$ purification opportunities, as purification may be applied to the input links prior to each swap and to the terminal link. Valid sequences are defined by the specific allocation of purification rounds to these opportunities limited by the available resource pool.

1) *Entanglement Generation Protocols*: We define an Entanglement Generation Protocol π as an ordered sequence of purification and entanglement swapping operations over the path P . The sequence of operations of a protocol π transforms the path P into a single virtual link generating an ensemble of indistinguishable entangled pairs ρ_π resulting in an end-to-end generation rate R_π (in Hz) and fidelity F_π . A protocol π operates on the batch of entangled pairs accumulated during a window T_w processing them during a time T_p^π .

2) *Entanglement Distribution Schemes*: An Entanglement Distribution Scheme S_P is defined by a set of Entanglement Generation Protocols $\Pi = \{\pi_1, \dots, \pi_m\}$ and a corresponding resource allocation vector, enabling the concurrent execution of multiple protocols across path P . Formally,

$\mathcal{S}_P = \{(\pi_j, \mathbf{R}_j)\}$, where $\mathbf{R}_j = (R_{\pi_j}^1, \dots, R_{\pi_j}^k)$ specifies the absolute resource consumption for protocol π_j . Each $R_{\pi_j}^i$ denotes the raw EGR drawn from physical link $e_i \in P$ to support protocol π_j . A distribution scheme \mathcal{S}_P effectively creates m distinct ensembles of entangled pairs (i.e. m distinct “flows”) yielding a product state $\rho^{\mathcal{S}_P} = \otimes_{i=1}^m \rho_{\pi_i}$ over a path P . An empty scheme $\mathcal{S}_P = \emptyset$ indicates an idle path.

C. Optimization Framework

An optimal solution for the Entanglement Distribution Problem is rarely confined to a single sequence of operations over a single path. Since entanglement purification is a non-linear operation where investing additional resources yields diminishing returns, the optimal strategy often involves a composite solution. Consequently, the Entanglement Distribution Problem must be optimized across multiple paths (utilizing disjoint or partially overlapping paths to aggregate capacity) and diverse Entanglement Generation protocols (executing heterogeneous sequences of operations). Thus, the challenge extends beyond simple shortest-path routing; it requires determining the optimal configuration of schemes \mathcal{S}_P across the set of all simple paths $\mathcal{P}_{s,d}$ between s and d to maximize resource utilization while strictly adhering to link capacity constraints.

We formulate the Entanglement Distribution Problem to maximize the aggregate capacity \mathcal{C} between s and d as:

$$\max_{\{\mathcal{S}_P\}_{P \in \mathcal{P}_{s,d}}} \sum_{P \in \mathcal{P}_{s,d}} \mathcal{C}(\rho^{\mathcal{S}_P}) \quad (4a)$$

subject to: Resource Constraint:

$$\sum_{P:e \in P} \sum_{\pi \in \mathcal{S}_P} R_{\pi}^e \leq r_e, \quad \forall e \in E. \quad (4b)$$

Non-negative Resource Consumption:

$$R_{\pi}^e \geq 0 \quad \forall e \in E, \quad \forall \pi \in \mathcal{S}_P. \quad (4c)$$

The objective function (4a) aggregates the capacities of all ensembles of entangled pairs generated across all active distribution schemes. The resource constraint (4b) ensures that the total physical consumption across all protocols using link e , denoted by R_{π}^e , does not exceed the available generation rate r_e . Finally, constraint (4c) forces R_{π}^e to non-negative values.

Note that, while quantum entanglement generation is a discrete process (counting individual pairs), our framework models $R_{\pi_j}^e$ as continuous variables. This relaxation is justified by the operational context of the network. As the system operates over a large number of synchronized accumulation windows T_w , the discrete pair counts are aggregated into a long-term average throughput. Furthermore, the Ensemble Capacity \mathcal{C} is an asymptotic metric defined over large ensembles of states. Therefore, treating R as a continuous flow variable accurately represents the steady-state performance of the multiple distribution schemes.

D. Problem Hardness and Intractability

The joint optimization of path selection and protocol configuration creates a nested combinatorial explosion that renders the problem intractable. First, the number of simple paths between a pair of nodes in a graph scales exponentially with the

network size (specifically, as $\mathcal{O}(|V|!)$ in dense graphs [44]). Second, for each candidate path P of length k , the optimizer must configure a valid Entanglement Generation Protocol π . On the one hand, the number of valid swapping operations grows following geometric permutations (specifically, as $\mathcal{O}(C_{k-1})$, where C is the Catalan number [45] and k is the number of links in the path), growing super-exponentially with path length. On the other hand, at each of the $2(k-1) + 1$ purification opportunities, we must assign a specific number of purification rounds. Third, since the purification strategy on one link changes the consumption requirements for all other protocols sharing that link, these decisions cannot be made in isolation. They are coupled globally via the link capacity constraints (Eq. (4b)). Finally, as established in Sec. IV, the capacity \mathcal{C} is strictly convex with respect to fidelity. However, the physical process of purification dictates that fidelity F and available rate R of entangled pairs are inversely related via a non-linear efficiency curve. To increase F , one must non-linearly decrease R . Consequently, the interplay of massive combinatorial search spaces, globally coupled constraints, and non-linear physical dynamics renders exact optimization computationally infeasible.

VI. CODE: SOLUTION PROPOSAL

To address the Entanglement Distribution Problem defined in the previous section, we propose a comprehensive optimization framework called **Capacity Optimization for Distributed Entanglement (CODE)**. To manage the inherent computational intractability of the problem, CODE employs a hierarchical solution strategy. First, it extracts a subset of candidate paths, $\mathcal{P}'_{s,d} \subseteq \mathcal{P}_{s,d}$. Second, it determines the optimal configuration scheme, \mathcal{S}_{P_i} , for every path $P_i \in \mathcal{P}'_{s,d}$.

The initial computation of $\mathcal{P}'_{s,d}$ mitigates the factorial complexity of path enumeration by restricting the search space to the N -shortest paths. The rationale behind this design decision, alongside the specific algorithmic details, is discussed in Sec. VI-E. Furthermore, to navigate the super-exponential solution space associated with \mathcal{S}_P , we adopt a hypergraph-based formulation. This abstraction effectively maps the combinatorial sequencing of quantum operations into a structured resource flow problem, enabling the application of Linear Programming (LP) techniques.

Constructing this hypergraph, however, presents significant structural challenges. In Sec. VI-A, we introduce a standard hypergraph formulation prevalent in related literature, followed by a critical analysis of its limitations (Sec. VI-A4). Most notably, standard approaches rely on strict fidelity discretization to maintain a finite graph size. This coarse approximation introduces systemic inaccuracies and artificially degrades the achievable end-to-end network performance.

To overcome these fundamental bottlenecks, we propose a novel *DP-based Hypergraph Generation Algorithm* (Sec. VI-B). By leveraging dynamic programming, this approach efficiently generates a pruned hypergraph that circumvents the deleterious effects of fidelity discretization. Building on this refined structure, Sec. VI-C formulates the corresponding LP, while Sec. VI-D provides a rigorous complexity

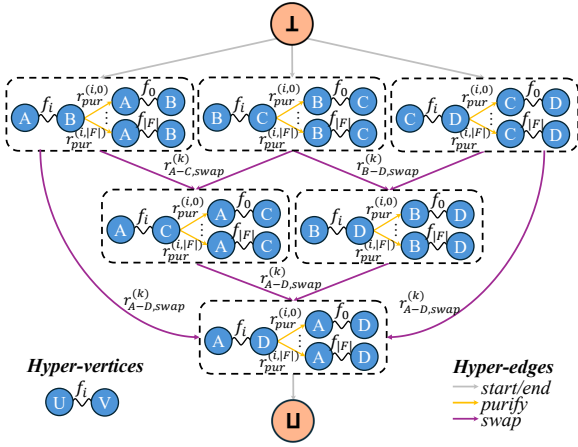


Fig. 2: Example of the directed graph \mathcal{L}_P for a path of 4 nodes and 3 links (A-B-C-D).

analysis. Finally, Sec. VI-E synthesizes these algorithmic components to present a complete overview of the CODE architecture, alongside practical system implementation details.

A. Hypergraph Formulation

To model the solution space, we build upon the state-of-the-art literature [12], [14] to construct a directed hypergraph $\mathcal{L}_P = (\mathcal{V}, \mathcal{E})$ that systematically encodes all feasible states of entanglement and the operational transitions between them. This abstraction maps the combinatorial complexity of the Entanglement Distribution Scheme into a navigable flow graph.

1) *Hyper-vertices (Entangled Links)*: The set of hyper-vertices \mathcal{V} encodes the possible states of entangled links between two specific nodes within a path P . Each hyper-vertex is a tuple (u, v, f) , representing an ensemble of indistinguishable EPs with fidelity f between nodes u and v on path P . If u and v are directly connected by an edge $e_{u,v} \in E$ in the physical topology, the entangled link is termed a *physical link*. Otherwise, we term it as a *virtual link*. Additionally, we define two auxiliary hyper-vertices: the source vertex (\perp) which represents the initial pool of raw resources over the path and the sink vertex (\sqcup) which represents the final successful distribution of end-to-end EPs.

2) *Hyper-edges (Sequences of operations)*: The set of hyper-edges \mathcal{E} models the transformation of a path P through a sequence of swapping and purification operations. We define a hyper-edge $\epsilon \in \mathcal{E}$ as a transition $(L, l_{\text{out}}, h, r_\epsilon)$, where $L \subseteq \mathcal{V}$ is the set of input hyper-vertices, l_{out} is the output hyper-vertex, and $h \in \{\text{swap}, \text{purify}, \text{start}, \text{end}\}$ is the operation type and r is the continuous consumption rate (Hz).

We distinguish between primary operations (swapping and purification, $|L| = 2$, denoted as l_1, l_2), which transform the state of existing entangled links, and auxiliary operations (initialization and termination, $|L| = 1$, denoted as l_1), which manage the flow of entanglement resources into and out of the quantum network. We mathematically formalize the primary operations as follows:

- 1) **Swapping (swap)**: Combines two links sharing an intermediate node into one link between non-adjacent nodes.

$$\text{swap}: \mathcal{V} \times \mathcal{V} \rightarrow \mathcal{V} \\ (u, v, f_1), (v, w, f_2) \mapsto (u, w, f_{\text{swap}}(f_1, f_2)) \quad (5)$$

Flow conservation requires equal consumption rate r from both inputs. Residual rates on non-bottleneck links remain available in the resource pool for concurrent operations.

- 2) **Purification (purify)**: Consumes two links between the same nodes to yield a single higher-fidelity link.

$$\text{purify}: \mathcal{V} \times \mathcal{V} \rightarrow \mathcal{V} \\ (u, v, f_1), (u, v, f_2) \mapsto (u, v, f_{\text{pur}}(f_1, f_2)) \quad (6)$$

Note that this formulation supports both symmetric (where input fidelities are identical, $f_1 = f_2$) and asymmetric purification (where $f_1 \neq f_2$).

The explicit functional forms of f_{swap} and f_{pur} are determined by the specific hardware implementation (see Sec. VII). Additionally, we formalize the two auxiliary functions to manage flow boundaries:

- 3) **Initialization (start)**: Maps the source vertex \perp to a set of physical link (u, v, f_0) , representing raw entanglement generation: $(\{\perp\}, (u, v, f_0), \text{start}, r)$.

- 4) **Termination (end)**: Maps end-to-end links (s, d, f) to the sink vertex \sqcup , representing protocol fulfillment: $(\{(s, d, f)\}, \sqcup, \text{end}, r)$.

3) *Hypergraph Structure*: The directed hypergraph $\mathcal{L}_P = (\mathcal{V}, \mathcal{E})$ represents the operational solution space, where a connected sequence of hyper-edges from source \perp to sink \sqcup defines an Entanglement Generation Protocol (π). To strictly model the physical constraints of entanglement swapping while ensuring that any spare capacity is preserved for other uses, we impose the following restrictions on the hypergraph:

Pair-wise Flow Conservation: A swapping hyper-edge consumes an identical flow rate r_ϵ from both input vertices. This reflects the physical reality that the end-to-end rate is strictly bounded by the link with the lower EGR.

Resource Pooling: Link vertices are modeled as cumulative resource pools. Multiple hyper-edges (representing distinct protocols) can draw from the same vertex. Physical validity is maintained by ensuring $\sum r_\epsilon \leq r_e$ for each link. This mechanism prevents the loss of “spare capacity” during asymmetric swaps, keeping residual EPs available for additional purification or parallel operations.

The Ensemble Capacity \mathcal{C} for a protocol is then derived from the terminal flow r_{end} and its associated fidelity f at the sink vertex \sqcup , following the definition provided in Sec. IV.

Fig. 2 depicts \mathcal{L}_P for a four-node path $P = \{A, B, C, D\}$. The source vertex \perp initiates entanglement distribution using physical links via the *start* operation. Dashed blocks represent fidelity manifolds for specific node pairs; within these, purification hyper-edges transition resource flow $r_{\text{pur}}^{(i,j)}$ toward higher-fidelity states. Swapping hyper-edges utilize $r_{u-v, \text{swap}}^k$ resources to execute pair-wise combinations of adjacent links: flow from (A, B) and (B, C) generates virtual links in (A, C) , which can then be combined with (C, D) to establish the end-to-end link (A, D) . The ensemble capacity is computed as

the final flow from the (A, D) block is directed to the sink vertex \sqcup through termination hyper-edges with EGR r_{end} . This configuration models all operational sequences as traversable paths within a unified flow graph.

4) *Hypergraph limitations*: Modeling entanglement rates as continuous variables yields a continuous fidelity manifold $f \in [0.5, 1]$, resulting in a hypergraph \mathcal{L}_P with an infinite vertex set. To tackle this problem, related literature [14] only considers a discrete set of fidelity values $\mathcal{F} = \{f_0, \dots, f_{|\mathcal{F}|}\}$ for every entangled link in \mathcal{L}_P . They approximate the resulting link fidelity values f to the largest $f_i \in \mathcal{F}$ s.t. $f \geq f_i$.

This approximation poses severe limitations. First of all, discretizing continuous fidelity values into predefined lower bounds forces physically distinct entangled pairs to share an identical fidelity representation. This uncertainty diminishes the overall system performance; since the capacity of the end-to-end ensemble is highly sensitive to fidelity, any inaccuracy in its measurement leads to sub-optimal configurations of the swapping and purification operations.

Second, discretization artificially degrades ensemble capacity by collapsing continuous fidelities into lower-bound intervals, rendering models insensitive to qualitative differences between paths. This creates a structural bias toward quantity over quality, where algorithms favor the highest raw entanglement rates while discarding lower-rate paths with superior true fidelities. Such sub-optimality compounds over multiple hops, systematically eliminating high-capacity trajectories. Furthermore, any attempt to mitigate this loss by increasing the resolution of the discrete set \mathcal{F} triggers a curse of dimensionality, reintroducing the very computational intractability the approximation sought to avoid.

B. DP-based Hypergraph generation algorithm

To address the fundamental limitations of the standard hypergraph formulation, we propose a novel hypergraph generation mechanism based on Dynamic Programming (DP). In contrast to prior approaches that force continuous quantum states into discrete values, our formulation explicitly preserves the exact, continuous fidelity values of the entangled pairs. Specifically, our DP-based algorithm constructs a pruned hypergraph that encapsulates only the most promising sequences of operations in terms of performance. By systematically filtering out sub-optimal configurations early in the process, this strategy effectively circumvents the curse of dimensionality, thereby substantially accelerating both the initial graph generation and the subsequent execution of the LP algorithm.

Crucially, this architecture relies on a decoupled optimization paradigm. The DP phase is designed exclusively to identify the maximum theoretical potential of isolated protocols. The subsequent LP formulation then leverages this solution space to determine the actual execution rates, globally optimizing the distribution schemes based on concurrent network demands and physical resource availability.

To systematically identify a set of high-performance protocols, direct maximization of the ensemble capacity cannot be

Algorithm 1

Hypergraph Construction via Dynamic Programming

Input: Network path P , set of physical links \mathcal{V}_L , physical link Entanglement Generation Rates $(\{r_l\}_{l=1}^{|P|-1})$, discrete fidelity levels \mathcal{F} , $\mathcal{L}'_P \leftarrow \emptyset$

Output: Pruned Hypergraph \mathcal{L}'_P

Notation: $l_{u,v}^i := (u, v, f^{(i)})$, where $f^{(i)} \in [f_i, f_{i+1})$

- 1: $\mathcal{V}' \leftarrow \mathcal{V}' \cup \{\perp, \sqcup\}$
- 2: **for** $l \in \mathcal{V}_L$ **do**
- 3: $\mathcal{V}' \leftarrow \mathcal{V}' \cup l$
- 4: $\mathcal{E}' \leftarrow \mathcal{E}' \cup (\{\perp\}, l, \text{start}, r_l)$
- 5: **end for**
- 6: **for** $\Delta = 2, \dots, |P| - 1$ **do**
- 7: **for** $u = 1, \dots, |P| - \Delta$ **do**
- 8: $v \leftarrow u + \Delta$
- 9: **for** $l_{u,w}^i, l_{w,v}^j \in \mathcal{V}'$ **do** \triangleright Perform Swap Operations
- 10: $f_{\text{new}} \leftarrow f_{\text{swap}}(l_{u,w}^i, l_{w,v}^j)$
- 11: $r_{\text{new}} \leftarrow \min(r_{e_{l_{u,w}^i}}, r_{e_{l_{w,v}^j}})$
- 12: Find k s.t. $f_{\text{new}} \in [f_k, f_{k+1}]$
- 13: **if** $r_{\text{new}} > r_{e_{l_{u,w}^i}}$ **then**
- 14: $\mathcal{V}' \leftarrow \mathcal{V}' \cup l_{u,v}^{\text{new}}$
- 15: $\mathcal{E}' \leftarrow \mathcal{E}' \cup (\{l_{u,w}^i, l_{w,v}^j\}, l_{u,v}^{\text{new}}, \text{swap}, r_{\text{new}})$
- 16: **end if**
- 17: **end for**
- 18: **for** $l_{u,v}^i, l_{u,v}^j \in \mathcal{V}'$ **do** \triangleright Perform Purify Operations
- 19: $f_{\text{new}} \leftarrow f_{\text{purify}}(l_{u,v}^i, l_{u,v}^j)$
- 20: $r_{\text{new}} \leftarrow \min(r_{e_{l_{u,v}^i}}, r_{e_{l_{u,v}^j}}) \cdot p_{\text{succ}}$
- 21: Find k s.t. $f_{\text{new}} \in [f_k, f_{k+1}]$
- 22: **if** $r_{\text{new}} > r_{e_{l_{u,v}^i}}$ **then**
- 23: $\mathcal{V}' \leftarrow \mathcal{V}' \cup l_{u,v}^{\text{new}}$
- 24: $\mathcal{E}' \leftarrow \mathcal{E}' \cup (\{l_{u,v}^i, l_{u,v}^j\}, l_{u,v}^{\text{new}}, \text{purify}, r_{\text{new}})$
- 25: **end if**
- 26: **end for**
- 27: **end for**
- 28: **for** $f_i \in \mathcal{F}$ **do**
- 29: $\mathcal{E}' \leftarrow \mathcal{E}' \cup (\{l_{s,d}^i\}, \sqcup, \text{end}, r_{l_{s,d}^i})$
- 30: **end for**
- 31: **end for**

employed, as this metric fails to satisfy the *optimal substructure property* required by the DP formulation¹ [46].

To circumvent this fundamental limitation, we reformulate the DP objective: rather than optimizing capacity directly, the algorithm maximizes the achievable Entanglement Generation Rate (EGR), denoted by r , for a discrete set of minimum fidelities $f \in \mathcal{F}$. This reformulation provides two pivotal advantages. First, it restores the requisite optimal substructure property, rendering a problem strictly solvable via DP. Second, it yields a diverse, Pareto-optimal frontier of high-performance solutions, as the algorithm naturally identifies the optimal

¹Consider an optimal end-to-end ensemble generated via a final purification step. The predecessor states (i.e., two lower-fidelity ensembles shared between the same nodes) are not necessarily optimal in terms of their individual capacities. Consequently, a globally optimal capacity cannot be reliably constructed from locally optimal capacity subproblems, violating the optimal substructure property.

Entanglement Generation Protocol for every minimum fidelity tier defined in \mathcal{F} . Specifically, we employ a ‘‘fidelity bucketing’’ strategy. For each predefined fidelity interval $[f_i, f_{i+1})$ (where f_i and f_{i+1} are consecutive values in \mathcal{F}), the algorithm identifies the optimal state tuple (u, v, f_{exact}) where $f_{\text{exact}} \in [f_i, f_{i+1})$ such as the associated EGR is the maximum within the interval $[f_i, f_{i+1})$.

Crucially, unlike standard discretization techniques that systematically round continuous fidelities down to predefined thresholds, our fidelity-bucketing strategy retains the true continuous value, f_{exact} , within each hyper-vertex. This ensures that all subsequent operations during the hypergraph construction leverage precise physical parameters rather than pessimistic lower-bound approximations. Consequently, the algorithm rigorously preserves the most promising operational sequences while effectively pruning suboptimal trajectories, ultimately maintaining a finite and computationally manageable graph without sacrificing the physical accuracy of the underlying quantum states.

Algorithm 1 details the pseudocode for the proposed DP-based hypergraph generation framework. The procedure starts with an initialization phase (lines 15), wherein the physical links (\mathcal{V}_L) are mapped to the source vertex \perp through the *start* operation. Following this, the algorithm systematically explores all combinations of sub-paths within path P via a set of nested iterations (lines 68). For each evaluated pair of nodes, the framework first considers entanglement swapping. It iterates over all available pairs of physical or virtual links (line 9) to establish a new end-to-end connection across an intermediate node. Upon computing the effective fidelity and EGR for a candidate swap (lines 1011), the algorithm executes the pruning step: if the candidate yields a strictly superior EGR for its specific fidelity interval, the newly generated virtual link is registered in the hyper-vertex set \mathcal{V}' (line 14), and its topological operation is appended to the hyper-edge set \mathcal{E}' (line 15).

Following this, an analogous dynamic programming recurrence is executed to assess purification operations (lines 1826). This step evaluates the distillation of available ensembles between the same node pairs, ensuring that all high-performing protocols are meticulously encoded into the final, computationally tractable hypergraph structure. To conclude, the established end-to-end pairs are mapped to the end hyper-vertex \sqcup through the *end* operation (lines 28-30).

By strictly restricting the graph topology to these optimal operational trajectories, our methodology achieves a profound reduction in computational complexity. Specifically, the number of hyper-edges is compressed from $\mathcal{O}(|V|^3|\mathcal{F}|^2)$ —the scaling characteristic of standard, unpruned formulations found in prior literature—to an upper bound of $\mathcal{O}(|V|^2|\mathcal{F}|)$. Crucially, this structural pruning is achieved without information loss; the framework retains the exact, non-discretized fidelity parameters strictly required for the accurate computation of the Ensemble Capacity.

C. Linear Programming Formulation

Using the previous pruned hypergraph $\mathcal{L}'_P = (\mathcal{V}, \mathcal{E})$, we formulate the Entanglement Distribution Problem presented

in Sec. V as a Linear Program (LP) optimization problem. For each hyper-edge $\epsilon = (S, l_{\text{out}}, h, r_\epsilon) \in \mathcal{E}$, r_ϵ is the decision variable associated to the number of Entangled Pairs generated by performing the corresponding operation $h \in \{\text{swap}, \text{purify}, \text{start}, \text{end}\}$. Let ρ_ϵ denote the quantum state of the EPs generated following ϵ . Then, the LP formulation of the Entanglement Distribution Problem is:

$$\max_{r_\epsilon, \epsilon \in \mathcal{E}} \sum_{\epsilon \in \mathcal{E}_{\text{end}}} \mathcal{C}(\rho_\epsilon) \cdot r_\epsilon \quad (7a)$$

$$\text{subject to: } \underline{\text{Flow Conservation:}} \quad \forall l \in \mathcal{V} \setminus \{\perp, \sqcup\}, \quad (7b)$$

$$\sum_{\epsilon \in \text{in}(l) \setminus \mathcal{E}_{\text{pur}}} r_\epsilon + \frac{1}{2} \sum_{\epsilon \in \text{in}(l) \cap \mathcal{E}_{\text{pur}}} p_{\text{succ}}(\epsilon) \cdot r_\epsilon \geq \sum_{\epsilon \in \text{out}(l)} r_\epsilon.$$

$$\underline{\text{Generation Limits:}}$$

$$\sum_{\epsilon \in \mathcal{E}_{\text{start}}(e)} r_\epsilon \leq r_e, \quad \forall e \in E. \quad (7c)$$

$$\underline{\text{Non-negative Resource Consumption:}}$$

$$r_\epsilon \geq 0, \quad \forall \epsilon \in \mathcal{E}. \quad (7d)$$

The objective function (7a) maximizes aggregate end-to-end Ensemble Capacity by summing terminal assigned execution rates r_ϵ weighted by their resulting state capacities $\mathcal{C}(\rho_\epsilon)$. Flow conservation (7b) maintains entanglement balance for each vertex $l \in \mathcal{V} \setminus \{\perp, \sqcup\}$ by requiring that total incoming entanglement rate—comprised of non-purification flow ($\text{in}(l) \setminus \mathcal{E}_{\text{pur}}$) and purification yields ($\text{in}(l) \cap \mathcal{E}_{\text{pur}}$) scaled by $\frac{1}{2}p_{\text{succ}}(\epsilon)$ where p_{succ} is the probability of successful purification—satisfies the total outgoing consumption in $\text{out}(l)$. This efficiency factor accounts for the physical sacrifice of two lower-fidelity pairs to produce one distilled pair. Generation limits (7c) enforce Resource Pooling by restricting the aggregate execution of initialization protocols in $\mathcal{E}_{\text{start}}(e)$ to the hardware generation rate r_e of physical link e . Finally, (7d) mandates non-negative execution rates r_ϵ to ensure physical feasibility.

D. Complexity Analysis

Related literature shows that a LP problems can be solved in polynomial time in the number of variables using interior-point methods [47]. Based on the formulation in (7), the number of variables in our approach corresponds to the edge count $|\mathcal{E}|$ of the graph \mathcal{L}_P . For an unpruned hypergraph \mathcal{L}_P , $|\mathcal{E}|$ is on the order of $\mathcal{O}(|V|^3|\mathcal{F}|^2)$, where $|V|$ represents the number of vertices in the path and $|\mathcal{F}|$ denotes the number of discrete fidelity values (Fidelity Resolution). While applying the pruning strategy reduces the variable count to $\mathcal{O}(|V|^2|\mathcal{F}|)$, it incurs a computational cost. The DP pruning algorithm is recurrent, operating on $|V|^2$ states represented by all possible pairs of link nodes. Each state evaluates two branch types: ‘‘swap’’ and ‘‘purify’’. The purify branch requires checking $|\mathcal{F}|^2$ states, while the swap branch requires checking $|V| \cdot |\mathcal{F}|^2$ states. Consequently, the total complexity of the DP pruning algorithm is $\mathcal{O}(|V|^3|\mathcal{F}|^2)$.

Despite the pruning algorithm having a complexity of $\mathcal{O}(|V|^3|\mathcal{F}|^2)$, this pre-processing step is computationally advantageous. The runtime of LP solvers, denoted as $\mathcal{C}_{LP}(N)$, generally scales super-linearly with the number of variables N

(often $O(N^{3.5})$ or higher for interior-point methods). Without pruning, the total cost is dominated by solving the LP with a large variable set: $\mathcal{C}_{LP}(|V|^3|\mathcal{F}|^2)$. In contrast, our approach incurs the additive pruning cost of $O(|V|^3|\mathcal{F}|^2)$ but reduces the optimization step to $\mathcal{C}_{LP}(|V|^2|\mathcal{F}|)$. Since the solver's complexity $\mathcal{C}_{LP}(N)$ grows significantly faster than linear time, the reduction in the dimensionality of the LP outweighs the overhead of the pre-processing algorithm.

E. CODE: Capacity Optimization for Distributed Entanglement

Having introduced the main building blocks of our solution, we unify the algorithmic components previously described into a cohesive orchestration framework termed CODE: Capacity Optimization for Distributed Entanglement.

To effectively manage the trade-off between the computational cost of graph construction and the necessity for low-latency responsiveness to user demands, CODE operates via a hierarchical control plane composed of two nested loops (see Alg. 2): the *Outer Loop* and the *Inner Loop*. This architectural separation ensures that computationally intensive tasks whose results can be stored and reused further, as long as the network state does not vary too much, are decoupled from real-time time-sensitive decisions.

1) *The Outer Loop*: The Outer Loop operates on a coarse time scale (ranging from seconds to minutes) and serves as the network's topological manager. Its primary objective is to monitor global network conditions—such as physical link availability, background noise levels, and long-term traffic patterns—and update the routing tables accordingly. In this phase, the control plane executes the computationally heavy pre-processing steps:

- 1) **Path Enumeration**: It deploys a modified Dijkstra algorithm to extract a candidate set of the N -shortest paths, $\mathcal{P}'_{s,d} \subseteq \mathcal{P}_{s,d}$, for all active source-destination pairs (s, d) .
- 2) **Protocol Optimization**: It executes the DP-based hypergraph generation algorithm (Sec. VI-B, Algorithm 1) across all candidate path $P \in \mathcal{P}'_{s,d}$ to identify the Pareto-optimal Entanglement Generation Protocols and evaluate the corresponding Ensemble Capacities of each protocol.
- 3) **Topological Pruning**: It filters the candidate set by retaining only the top- K paths ($\mathcal{P}_K \subseteq \mathcal{P}'_{s,d}$). In particular, we select the K paths with the highest Ensemble Capacity of their best performing Entanglement Generation Protocols, discarding the $N - K$ underperforming paths.
- 4) **Hypergraph Synthesis**: It aggregates the DP-optimized operational sequences derived from the selected \mathcal{P}_K paths to construct and cache the global, multi-path pruned hypergraph, $\mathcal{L}'_{\mathcal{P}_K}$.

2) *The Inner Loop*: The Inner Loop operates on a fine time scale (10ms to 1s) and handles near-instantaneous user requests and rapid fluctuations in demand. Unlike the outer loop, which addresses structural optimization, the inner loop focuses purely on flow maximization. When a transmission request arrives, the Inner Loop retrieves the pre-computed pruned hypergraph $\mathcal{L}'_{\mathcal{P}_K}$ and solves the LP to determine the optimal Entanglement Distribution Scheme.

Algorithm 2

CODE: Capacity Optimization for Distributed Entanglement

Input: Network topology G , noise sources (Sec. VII), traffic patterns, N (paths), K (top paths), T_{outer} (Update period)
Output: Optimal Entanglement Distribution Scheme

```

1: while Network is active do                                ▷ Outer Loop
2:   Monitor physical link availability
3:   for each active source-destination pair  $(s, d)$  do
4:      $\mathcal{P}_N \leftarrow$  runModifiedDijkstra( $G, s, d, N$ )
5:     for each path  $p \in \mathcal{P}_N$  do
6:        $\{C_i\}_{i=1}^N \leftarrow$  EC estimation via DP (Sec. VI-B)
7:     end for
8:      $\mathcal{P}_K \leftarrow$  selectTopKPaths( $\mathcal{P}_N, \{C_i\}_{i=1}^N, K$ )
9:      $\mathcal{L}'_{\mathcal{P}_K} \leftarrow$  generatePrunedHypergraph( $\mathcal{P}_K$ )
10:    end for
11:    Store  $\mathcal{L}'_{\mathcal{P}_K}$  for real-time access
12:    while  $t_{current} < T_{outer}$  do                            ▷ Inner Loop
13:      if Transmission request arrives then
14:        Retrieve stored hypergraph  $\mathcal{L}'_{\mathcal{P}_K}$ 
15:         $S_{\mathcal{P}_K} \leftarrow$  runLP( $\mathcal{L}'_{\mathcal{P}_K}$ )
16:        Execute  $S_{\mathcal{P}_K}$ 
17:      end if
18:    end while
19:  end while

```

This hierarchical approach offers a distinct computational advantage. By relegating the $\mathcal{O}(|V|^3|\mathcal{F}|^2)$ complexity of the DP-based pruning to the background Outer Loop, the critical path of the request processing is limited to solving the LP over a significantly reduced variable set. This ensures that the network can optimize entanglement distribution in near-RT without being bottlenecked by the combinatorial explosion of the full protocol space.

VII. EVALUATION FRAMEWORK

This section details the building blocks of our evaluation framework. This environment provides a unified reference to characterize how entanglement is generated and distributed across Quantum Networks. Developed in Python via the Net-Squid [48] library, the platform allows for the high-fidelity representation of scalable quantum networks. Unlike simplified models, our approach explicitly accounts for entanglement generation, swapping, and purification under realistic noise and hardware constraints.

A. Quantum Network

We model each node of the quantum network as a quantum repeater equipped with a Spontaneous Parametric Down Conversion (SPDC) source capable of generating entangled polarized photons encoding qubits. Quantum nodes can store qubits in quantum memories and perform computing operations via quantum gates and measurements on them, enabling Bell-State Measurements for quantum teleportation. Adjacent quantum nodes are connected via fiber-optic channels that enable the exchange of entangled photon pairs to establish entanglement through shared entangled pairs, enabling quantum teleportation

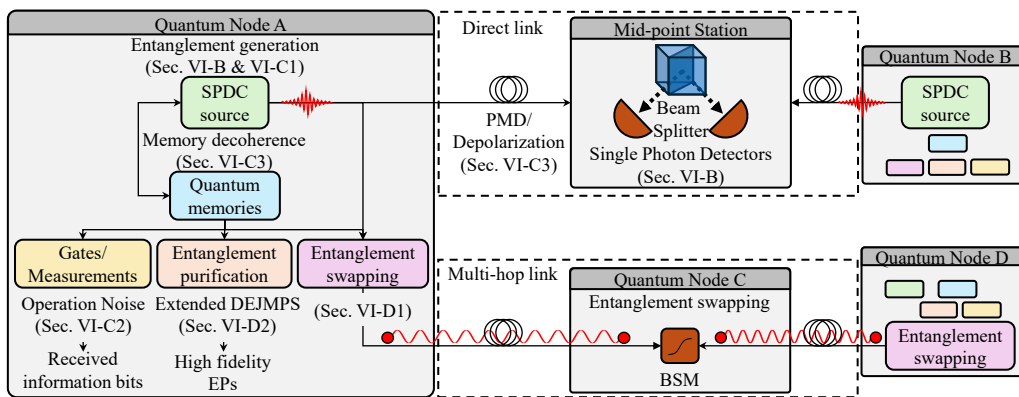


Fig. 3: Schematic representation of the Quantum Network system model used in the performance evaluation.

of arbitrary states (Fig. 3 *Direct link*). Non-adjacent nodes can become entangled via sequential swapping operations across intermediate nodes, extending communication over long distances (Fig. 3 *Multi-hop link*). All these operations are subject to imperfections and noise. To mitigate any source of fidelity degradation, quantum nodes can also perform entanglement purification operations. Fig. 3 shows the different building blocks of our QN and the noise effects we have considered.

1) *Orchestration and Control Framework*: A classical network overlaid on the QN interfaces with the quantum nodes using a centralized network controller. This controller enables the synchronization and coordination of quantum protocols. It is divided into two main control loops: (i) a Non-Real-Time (non-RT) control loop that manages entangled resources and high-level policies (e.g. signaling link failures) with execution latencies exceeding 1s, and (ii) a Near-Real-Time (near-RT) control loop which periodically reconfigures the quantum network and synchronizes the execution of different Entanglement Generation Protocols with response times ranging from 10ms to 1s. The controller ensures that the maximum processing time of all Entanglement Generation Protocols T_p^π is lower than the accumulation time window T_w . Furthermore, it ensures that $T_p^\pi + T_w$ does not exceed the quantum memories' coherence time (see Sec. VII-C3).

B. Entanglement generation

To model entanglement generation, we adopt the mid-point link-level procedure presented in [49] and depicted in Fig. 3 under the *direct link* representation. Adjacent nodes store one photon from an SPDC-emitted pair and transmit the other to a mid-station. Successful entanglement is heralded by coincident detections after photons interfere at the mid-station's polarizing beam splitter.

At each quantum node, we model the effective local EGR at zero distance as r_{local} . This parameter accounts local hardware efficiencies including the probabilities of single-photon emission, memory-photon coupling and detector efficiency [50]–[52]. Consequently, the effective entanglement generation rate between adjacent nodes separated by a distance L is determined by the fiber transmission loss as

$$r_{\text{link}}(L) = r_{\text{local}} \cdot e^{-\alpha L/10}, \quad (8)$$

where α represents the optical fiber attenuation coefficient. We used an attenuation coefficient $\alpha = 0.21$ dB/Km [48].

C. Entanglement Fidelity in Noisy Environments

The quality of a shared entangled pair can be quantified using its fidelity, which measures how close the actual state is to a target Bell state (see Sec. III). Several noise sources contribute to the degradation of entanglement fidelity.

1) *Initial Fidelity of Generated Entangled Pairs*: The initial fidelity of a two-photon state, measured immediately after generation with respect to an ideal Bell state and denoted as F_0 , is typically observed to be slightly below unity due to imperfections in the generation process. Experimental results indicate that $F_0 \simeq 0.98$ is a conservative estimate for high-quality SPDC implementations [53], [54].

2) *Imperfect Local Operations and Measurements*: Local operations such as quantum gates and measurements inevitably introduce inaccuracies and noise degrading entanglement fidelity and limiting communication performance. Also, these imperfections directly affect entanglement swapping and purification operations. We model these imperfections adopting the approach introduced in [6]:

- **Quantum gate model**: We model a single-qubit gate noise using a parameter $p_1 \in [0, 1]$, representing the lower bound on the probability of ideal operation. With probability $1 - p_1$, the noisy gate replaces the qubit with a maximally mixed state. Thus, the action of a noisy gate on a multi-qubit state ρ is described as:

$$\rho \mapsto \underbrace{p_1 O_1^{\text{ideal}} \rho}_{\text{Ideal operation}} + \underbrace{\frac{1-p_1}{2} \text{Tr}_1\{\rho\} \otimes \mathbb{I}_1}_{\text{Depolarizing noise}}, \quad (9)$$

where O_1^{ideal} is the single-qubit ideal quantum gate and \mathbb{I}_1 is the maximally mixed state on the affected qubit. Two-qubit gates are modeled analogously with reliability parameter p_2 , and the depolarized component is replaced by a maximally mixed state on the involved qubits.

- **Measurement model**: We model imperfect quantum state measurements using Positive Operator-Valued Measures (POVMs) [55] with an accuracy parameter $\eta \in [0, 1]$, representing the probability of correctly identifying the

qubit state. For a single-qubit measurement in the computational basis $\{|0\rangle, |1\rangle\}$, the noisy measurement operators are defined as:

$$P_0^\eta = \underbrace{\eta|0\rangle\langle 0|}_{\text{Correct identification}} + \underbrace{(1-\eta)|1\rangle\langle 1|}_{\text{Misidentification}}, \quad (10)$$

$$P_1^\eta = \underbrace{\eta|1\rangle\langle 1|}_{\text{Correct identification}} + \underbrace{(1-\eta)|0\rangle\langle 0|}_{\text{Misidentification}}. \quad (11)$$

In quantum teleportation, Bell-State Measurements (BSMs) project two qubits onto one of the four Bell states. We model BSMs using an imperfect two-qubit CNOT gate followed by a Hadamard operation and two noisy single-qubit measurements as defined above. Experimental works on quantum gates and measurement fidelities in superconducting and spin-based quantum hardware [52], [56]–[58] report reliability and accuracy parameters of $\eta = p_1 = p_2 = 0.995$.

3) *Decoherence in Quantum Memories*: Environmental noise degrades the fidelity of stored quantum states in quantum memories via two processes [59]: (i) thermal decoherence (i.e. amplitude damping), characterized by the relaxation time T_1 , and (ii) dephasing, characterized by the coherence time T_2 . Quantum states are assumed to remain coherent and unaffected by noise up to a fixed maximum storage time t_{cut} , beyond which they are considered fully decohered [10], [12], [22]. This approximation is well-justified by the significant gap between the experimentally measured coherence durations [60], [61] ($T_1 = 3600$ s, $T_2 = 1.46$ s) and typical quantum protocol execution times on the order of $\sim 10^{-2}$ seconds [6].

4) *Depolarization in Optical Fiber*: A polarization-encoded photon propagating through an imperfect optical fiber experiences a relative time delay denoted by τ_{PMD} between orthogonal polarization states. This phenomenon is referred as Polarization Mode Dispersion (PMD) [50] and is the primary source of fidelity degradation. When τ_{PMD} exceeds the photon's coherence time τ_{coh} , polarization coherence is lost.

We model τ_{PMD} as a normally distributed random variable [43], [50], $\tau_{\text{PMD}} \sim \mathcal{N}(DGD \cdot \sqrt{L}, DGD \cdot \sqrt{L})$ where the DGD is the differential-group delay in ps/ $\sqrt{\text{Km}}$ and L is its length of the fiber in Km. Experimental works [50] estimate the DGD of a single-mode fiber to be around 0.1 ps/ $\sqrt{\text{Km}}$ and a coherence time τ_{coh} of 1.6 ps.

D. Long-Distance Entanglement Distribution

1) *Entanglement Swapping*: Realistic swapping operations yield an entangled state of reduced fidelity due to imperfections and noise. After $N - 1$ consecutive swapping operations across a N hops, the resulting fidelity F' of an EP is given by

$$F' = \frac{1}{4} \left[1 + 3 \left(p_1^2 p_2 \cdot \frac{4\eta^2 - 1}{3} \right)^{N-1} \prod_{i=1}^N \left(\frac{4F_i - 1}{3} \right) \right], \quad (12)$$

where p_1 , p_2 , and η denote the reliabilities of the local operations and measurements and F_i denotes the fidelity after the i -th swapping operation [38]. (We assume p_1 , p_2 and η equal for all network nodes in eq. (12)). This expression highlights

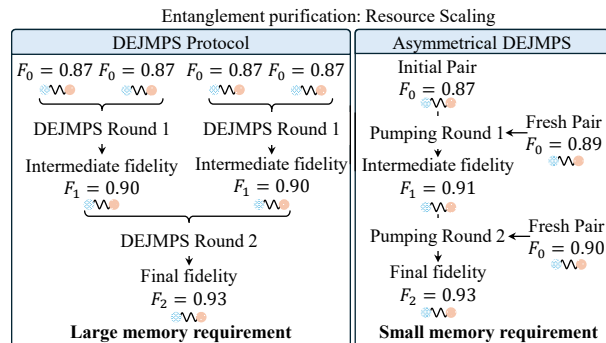


Fig. 4: DEJMPS and Asymmetrical DEJMPS protocols.

that unless each operation and link is performed with near-perfect accuracy, the final fidelity F' decays exponentially with the number of swaps, asymptotically approaching $1/4$. This emphasizes the need of purification operations at intermediate nodes to enable long-distance entanglement distribution.

2) *Entanglement Purification*: Entanglement purification is performed iteratively in discrete rounds, in which multiple low-fidelity pairs are combined to produce a smaller number of higher-fidelity pairs. Purification employs local quantum gates and measurements to decide whether the resulting pair is kept making the protocol inherently probabilistic. Fidelity gains diminish over successive rounds, asymptotically approaching a maximum attainable value $F^{\text{max}}(p_1, p_2, \eta) < 1$. In this work, we utilize the DEJMPS protocol [62], and extend it, via relaxing the identical-fidelity requirement, to an asymmetrical variant that allows for lower resource consumption.

DEJMPS Protocol: The DEJMPS purification protocol [62] operates on pairs of shared entangled particles with identical fidelities between two nodes (i.e. a transmitter and a receiver). Both apply to the pair local unitary rotations, followed by CNOT operations and a local measurement of one shared qubit in the computational Z basis. Both nodes retain the remaining pair only if both parties obtain identical measurement outcomes. The protocol is fidelity-optimal for two copies of Bell diagonal states of rank up to three, achieving the maximum possible output fidelity and success probability [63]. The protocol succeeds with probability (assuming p_1 , p_2 , and η equal for both nodes)

$$p_{\text{succ}} = \frac{1}{18} (9 + (4F_1 - 1)(4F_2 - 1)(1 - 2\eta)^2 p_2^2), \quad (13)$$

where F_1 and F_2 are the fidelities of the input pairs. The fidelity of the retained pair after successful purification is

$$F' = \frac{9 + p_2^2 ((1 - 8F_2) - 8F_1(6\eta^2 + 6\eta - 1))}{72 \cdot p_{\text{succ}}} + \frac{16p_2^2 F_1 F_2 (12\eta^2 - 12\eta + 5)}{72 \cdot p_{\text{succ}}} \quad (14)$$

DEJMPS's identical input fidelity constraint causes the expected number of consumed pairs to grow exponentially, scaling as $(2/p_{\text{succ}})^{k_{\text{max}}}$ for k_{max} rounds. This exponential resource scaling (see Fig. 4) poses a limitation in scenarios with constrained qubit memory.

TABLE I: Solution characterization across varying paths with capacity improvement relative to Rate-DP.

#	Strategy	Performance Metrics			Operational Metrics			Capacity Improv.
		EGR	Fidelity	Capacity	Swaps	Purif.	Pairs	
3	Rate-DP	2918.27	0.9266	1610.62	1.00	0.57	1.00	—
	Rate-LP	2920.20	0.9243	1584.53	1.20	1.70	1.20	-1.62%
	EC-LP	2920.20	0.9266	1614.89	1.78	1.24	1.78	+0.27%
	CODE	2920.20	0.9343	1738.62	1.80	1.41	1.80	+7.95%
5	Rate-DP	1902.40	0.8863	644.38	3.00	4.11	1.00	—
	Rate-LP	1971.85	0.8784	602.96	6.78	7.31	1.24	-6.43%
	EC-LP	2078.68	0.8800	666.59	9.46	6.16	3.19	+3.45%
	CODE	2163.37	0.8921	825.50	8.71	5.38	3.20	+28.11%
7	Rate-DP	704.13	0.8760	191.34	5.00	12.05	1.00	—
	Rate-LP	778.71	0.8701	185.70	19.41	21.78	1.01	-2.95%
	EC-LP	845.64	0.8678	194.29	18.99	19.05	3.36	+1.55%
	CODE	1117.58	0.8723	290.13	17.01	14.84	3.82	+51.63%
10	Rate-DP	276.11	0.8739	70.09	8.00	23.69	1.00	—
	Rate-LP	306.96	0.8700	72.60	39.67	51.99	1.00	+3.58%
	EC-LP	308.08	0.8709	73.21	38.11	48.74	3.50	+4.44%
	CODE	522.35	0.8721	127.15	28.99	35.36	3.90	+81.39%

Asymmetrical DEJMPS: The asymmetrical variant is an adaptation of entanglement pumping [6] that relaxes the identical-fidelity requirement. It utilizes the same sequence of operations as the symmetrical case—and thus follows the same physical models for p_{succ} and F' —but allows for $F_1 \neq F_2$. Typically, a high-fidelity "protected" pair is iteratively purified by consuming a fresh, lower-fidelity "source" pair. While the single-step performance is upper-bounded by the symmetrical case, the asymmetrical approach allows for linear scaling of memory resources relative to the number of rounds.

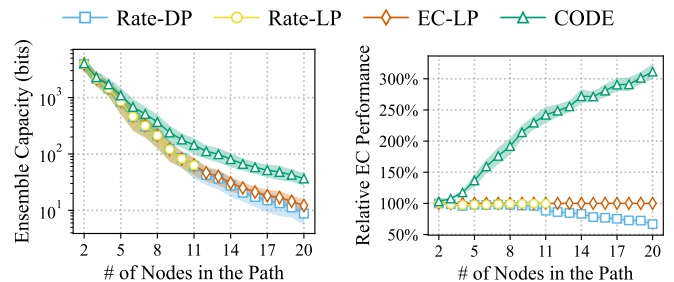
VIII. PERFORMANCE EVALUATION

This section evaluates CODE against state-of-the-art solutions (Sec. VIII-A, VIII-B). The analysis covers Ensemble Capacity performance (Sec. VIII-B1), operational optimization (Sec. VIII-B2), and scalability (Sec. VIII-B3). It assesses benchmark solution sensitivity to the minimum fidelity lower bound (Sec. VIII-C), comparing optimal selections against CODE. Finally, it quantifies computational scalability (Sec. VIII-D), comparing CODE's execution times against benchmarks across varying fidelity discretization (Sec. VIII-D1) set sizes, path lengths (Sec. VIII-D2), and network sizes (Sec. VIII-D3). Our solution and benchmarks results use the evaluation framework described in Sec. VII. We implemented CODE using Python, the evaluation framework using NetSquid, and we used Gurobi as the main solver for any Linear Programming (LP) formulation.

A. Solution Benchmarks

State-of-the-art solutions to the Entanglement Distribution Problem do not optimize the Ensemble Capacity, rather they maximize the Entanglement Generation Rate (EGR) subject to minimum fidelity constraints. Thus, to fairly compare CODE against state-of-the-art solutions, we adapt them using a fixed fidelity lower-bound f_{LB} and compute the resulting capacity using the end-to-end EGR. Selecting the optimal f_{LB}^* is non-trivial due to the complex, non-linear trade-offs between fidelity and generation rates (see Sec. VIII-B). We compare CODE against the following three strategies:

- *Rate-DP:* This solution is based on the Dynamic Programming (DP) formulation presented in [14]. It maxi-



(a) Ensemble Capacity (b) Relative EC Gains

Fig. 5: Comparison of the Ensemble Capacity and Relative Ensemble Capacity Gains as a function of the path length.

mizes the EGR subject to a minimum fidelity constraint, restricted to entanglement pumping for purification.

- *Rate-LP:* This solution is based on the Linear Programming (LP) formulation presented in [14]. It computes the hypergraph using the standard framework presented in Sec. VI-A and maximizes the EGR subject to a minimum fidelity constraint.
- *EC-LP:* This solution maximizes the Ensemble Capacity via the LP formulation presented in Sec. VI-C building a hypergraph using the standard framework presented in Sec. VI-A. This solution acts as an ablation study on the efficacy of DP-based hypergraph generation.

In order to get meaningful operational insights, we evaluate CODE and the benchmark solutions over realistic network topologies from TopoHub [64]. This repository provides Gabriel graph models [65], characterizing the proximity-based connectivity inherent in fiber-optic deployments, alongside empirical topologies from The Internet Topology Zoo [66].

B. Performance Benchmarking

We evaluate CODE and the benchmark solutions using a 1000-node Gabriel graph from the TopoHub repository [64]. For each network link, distances are uniformly sampled from the range [20, 150] km. The local EGR at zero distance (r_{local}) is set to 12k entangled pairs per second (EPs/s) [50] for all nodes. For the *Rate-DP* and *Rate-LP* solutions, we fix the fidelity lower bound at $f_{LB} = 0.87$ (more details in Sec. VIII-C). To ensure a fair comparison, all solutions were evaluated over a discrete set of fidelity values of size $|\mathcal{F}| = 100$. We evaluate the solutions of different approaches across 100 randomly selected node pairs for each path length (including both end nodes) of 3, 5, 7, and 10 nodes (corresponding to 2, 4, 6, and 9 hops, respectively).

Table I summarizes the averaged performance and operational metrics. Performance metrics include the mean end-to-end EGR, mean fidelity, and average Ensemble Capacity. Operational metrics encompass the average number of entanglement swaps and purification rounds required by the distribution scheme, alongside the mean number of distinguishable EPs produced. The final column reports the relative capacity improvement compared to the *Rate-DP* benchmark.

1) *Ensemble Capacity Optimization:* The results presented in Table I show that CODE achieves better Ensemble Capacity optimization across all path lengths. While it provides a

modest 7.95% improvement in 3-hops paths, its improvement scales dramatically to a 81.39% capacity increase in 10-hop paths. Also, CODE achieves the highest end-to-end EGR and top-2 fidelity across all path lengths. Since CODE utilizes the discretization set \mathcal{F} as interval boundaries, it accesses a richer search space of Entanglement Distribution Schemes, identifying high-potential solutions that standard methods would otherwise prematurely prune.

On the other hand, *EC-LP* consistently delivers higher EGR than both *Rate-DP* and *Rate-LP* as it aggressively uses residual resources to maximize the Ensemble Capacity. Conversely, despite optimizing a superset space of *Rate-DP* [14], *Rate-LP* unexpectedly underperforms *Rate-DP* in capacity for medium-to-short chains. In these scenarios, *Rate-LP* suffers from a “high-rate, low-fidelity” trade-off; the solver selects high EGR solutions that are undermined by poor end-to-end fidelity.

2) *Operational Optimization*: Operationally, CODE generates a highly heterogeneous ensemble of end-to-end entangled pairs (EPs). By optimizing residual resources, it maximizes EPs yield while maintaining the number of swap and purification operations comparable to benchmark solutions. While *EC-LP* also produces high-utility heterogeneous ensembles, it achieves lower total capacity than CODE. Conversely, as *Rate-DP* is constrained by a single distribution protocol, it limits purification opportunities and ties swap counts to path length. *Rate-LP* is operationally inefficient, performing additional swapping and purification operations that fail to increase the ensemble size significantly beyond *Rate-DP* levels.

3) *Scaling with Path Length*: To evaluate solution scalability, we analyze performance as path length increases. We now use the real link distances of the 1000-node Gabriel graph. Link distances range from 25 to 400 km with a mean 100 km. As previously established, we randomly select node pairs spanned by defined path lengths. Figure 5a presents the 95% confidence interval for Ensemble Capacity computed across 20 distinct paths per length size as a function of node count. To isolate algorithmic efficiency from path-dependent variables (e.g., total length, Entanglement Generation Rate, and intermediate link fidelity), Figure 5b displays the Relative EC Performance. This secondary analysis normalizes each method against the *EC-LP* benchmark on a per-path basis. *EC-LP* serves as the 100% baseline due to its consistently superior performance among state-of-the-art methods. For *Rate-LP* solution we cannot use paths with more than length 10 as we exhaust our available memory to run the solution.

We observe that the absolute Ensemble Capacity of all four solutions decreases as the path length grows. This behavior aligns with physical expectations: longer paths require more entanglement swapping and purification operations inevitably leading to accumulated fidelity degradation and lower effective EGR across the end-to-end connection.

CODE consistently outperforms the other methods across all path lengths, yielding the highest overall capacity and exhibiting the most resilience to network scaling. While it shows a modest improvement over the *EC-LP* at a 2-node configuration, its relative advantage scales steadily, achieving over a 300% performance gain at 20 nodes path length.

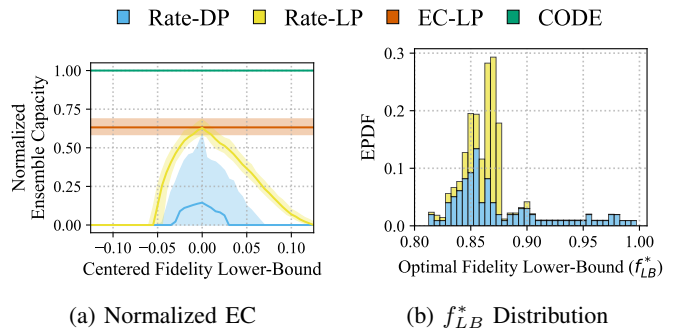


Fig. 6: Impact of the f_{LB} on network performance.

C. Fidelity Lower-Bound Sensitivity

We now evaluate the sensitivity of benchmark’s results to fidelity lower bound constraint. Even though CODE does not depend on the fidelity lower bound constraint as it optimizes directly the Ensemble Capacity, it is helpful to study how sensitive state-of-the-art solutions are to this constraint as its value largely affect the quality of solutions. To study this dependence, we resort to the Gabriel graph used in Sec VIII-B1, and run the CODE and the benchmark solutions for f_{LB} values between 0.815 and 0.995 in 0.005 increments. We analyze the results for 100 randomly selected pairs of nodes connected between a path with lengths between 2 to 10 hops. Fig. 6a plots the normalized Ensemble Capacity metric as a function of the centered fidelity lower-bound, $f_{LB}^c = f_{LB} - f_{LB}^*$ where $f_{LB}^* = 0.87$ maximizes the Ensemble Capacity for *Rate-DP* and *Rate-LP*. Centering the fidelity decouples intrinsic protocol performance from the path-dependent optimal operating points of the benchmarks. Per-path normalization of the Ensemble Capacity (EC) values isolates topological variability, allowing for a fair cross-scenario comparison. Also, CODE’s capacity defines the EC normalization baseline.

As we observe in Fig.6a, CODE directly optimizes the Ensemble Capacity without a fixed fidelity constraint, its performance is strictly invariant to f_{LB} . *EC-LP* solution is the closest benchmark to CODE, achieving approximately 65% of CODE’s capacity while also remaining invariant to f_{LB} . This performance gap highlights the limitations inherent in the standard hypergraph models utilized by *EC-LP*. By avoiding the rigid fidelity discretization characteristic of prior art, CODE accesses a richer search space of Entanglement Distribution Schemes, exploiting high-potential solutions that standard discretization methods prematurely prune.

Conversely, the *Rate-DP* and *Rate-LP* approaches exhibit a distinct Gaussian-like sensitivity to f_{LB} . Their performance depends heavily on the precise optimization of f_{LB} , a non-trivial task dependant on multiple path-specific factors, including link count, link-level fidelities, and EGRs. Consequently, no single fidelity lower-bound is universally optimal across diverse network configurations. Figure 6b presents the distribution of optimal values (f_{LB}^*) for the *Rate-DP* and *Rate-LP* solutions across multiple Gabriel topologies and path lengths. Although the f_{LB}^* values are distributed within the interval (0.8, 1.0), benchmark performance exhibits strong sensitivity to the exact selection of f_{LB} . A marginal deviation of 0.02 from f_{LB}^* yields up to a 20% degradation in EC.

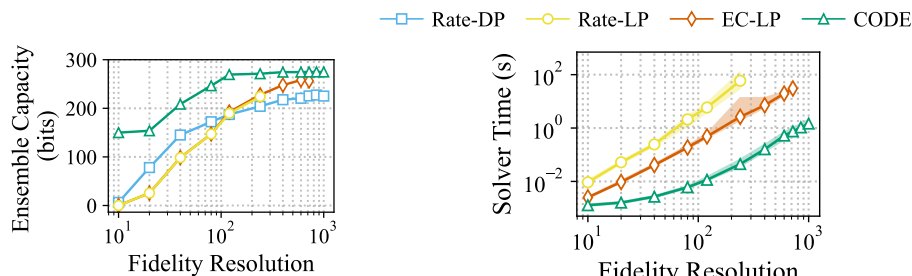


Fig. 7: Ensemble Capacity as a function of the Fidelity Resolution.

D. Computational Scalability Analysis

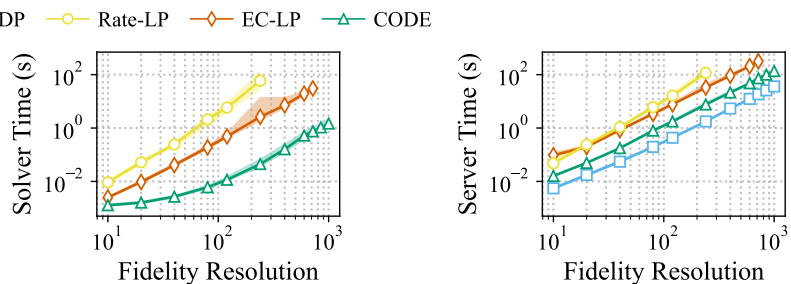
Finally, we evaluate the computational scalability of CODE against the stat-of-the-art solutions. We analyze the execution time as a function of the fidelity resolution—defined as the discretization set cardinality, $|\mathcal{F}|$ —and the total number of nodes in the path and network. Quantifying these computational trade-offs delineates the operational limits of the benchmark formulations and validates CODE’s applicability for large-scale quantum network deployments.

1) *Fidelity Discretization*: To begin with, we evaluate the sensitivity of the execution time of the different solutions to the fidelity resolution. As explained in Sec. VI $|\mathcal{F}|$ sets the size and precision of the state space during the hypergraph construction. A higher resolution allows for a more accurate tracking of entanglement states, which enables the discovery of higher-yield routing solutions. However, this comes at the cost of a larger state space, increasing the computational burden (see Sec. VI-D). We evaluate the impact of Fidelity resolution using a 1000-node Gabriel graph from TopoHub repository [64]. We now fix the path length to 6 nodes and study the effect of the fidelity resolution in the output EC.

Figure 7 depicts the Ensemble Capacity as a function of Fidelity Resolution. As expected, all solutions exhibit an increase in capacity as the resolution becomes higher. The state-of-the-art benchmarks start with near-zero capacity at low resolution and require highly refined state spaces to identify viable entanglement distribution schemes. In contrast, CODE demonstrates remarkable algorithmic efficiency at low resolutions. It achieves near-peak capacity at a resolution of just 10^2 , while the competing methods must scale toward 10^3 to reach comparable, albeit still inferior, performance levels.

Fig. 7a presents the Solver Time which is time required for the LP solver to find the optimal solution while fig. 7b presents the Server Time which is time required to construct the state space and optimization model. Both plots display the 1st, 50th, and 99th percentiles. *Rate-DP* is exclusively plotted in the Server Time figure as it lacks a distinct Solver phase.

Solver and Server Times scale with increasing fidelity resolution, aligning with the theoretical predictions in Sec. VI-D. High-resolution operation ($|\mathcal{F}| = 10^3$) yields execution times several orders of magnitude longer than lower settings. This creates a severe scalability bottleneck for the benchmark methods, which require high-resolution to achieve meaningful Ensemble Capacity solutions. At these scales, benchmark Solver Times exceed quantum memory coherence times, ren-



(a) Solver Time (b) Server Time
Fig. 8: Running time analysis as a function of the Fidelity Resolution.

dering them unfeasible for responsive network management. Conversely, CODE bypasses this limitation by extracting near-optimal solutions at a coarser resolution ($|\mathcal{F}| = 10^2$). At this resolution, CODE’s Solver Time remains near 10^{-2} s, keeping Server Time sufficiently low to enable rapid network updates.

2) *Path Length*: Next, we evaluate how execution times change as a function of the number of nodes in a path. Using the previous section results, we fix $|\mathcal{F}| = 100$ across all solutions and run them for paths lengths from 2 to 20 nodes using the same graph. Figure 9 presents the 99th, 50th, and 1st percentiles of both Server and Solver Time. As noted previously, *Rate-DP* appears only in the Server Time plot.

From fig. 9b, we see that *Rate-DP* exhibits the fastest Server Time among the four solutions. However, as previously explained, this lower computational overhead comes at the expense of a significant performance degradation (see Sec. VIII-A). *Rate-LP* exhibits the worst server time scalability; its computational cost compounds so aggressively that it mimics exponential scaling before becoming entirely unfeasible for path lengths higher than 11 nodes. CODE shows better Server Times than *Rate-LP* and *EC-LP* solutions. It demonstrates lower Server Times than both, processing 20-node paths in approximately 10^2 seconds in the worst-case scenario. Since CODE meticulously constructs a pruned hypergraph via DP, its Server Time absorbs an initial overhead that the standard LP approaches do not.

The true impact of CODE’s DP hypergraph generation can be clearly visualized in fig. 9a. CODE’s solver time scales exceptionally well, remaining safely bounded between 10^{-3} and 10^{-1} seconds. Even at the maximum path length, it operates an order of magnitude below the quantum memory decoherence time and its inner loop latency limit of 1s. As both *Rate-LP* and *EC-LP* use an unpruned hypergraph, they scale worse than CODE. Their Solver Time increases rapidly, breaching the 1s operational latency limit at a path length of 5 nodes for *Rate-LP* and 8 nodes for *EC-LP*.

3) *Network Size*: Finally, we examine CODE’s performance across networks of different network sizes. We conducted extensive experiments using network topologies ranging from 100 to 900 nodes. For each topology, we evaluated 700 randomly selected source-destination pairs, selecting the top 3 shortest paths between them. Fig. 10 depicts the Server and Solver Times as scatter plots to illustrate the distribution of execution times with a marker in the median performance.

CODE’s Server Time ranges from approximately 10^0 sec-

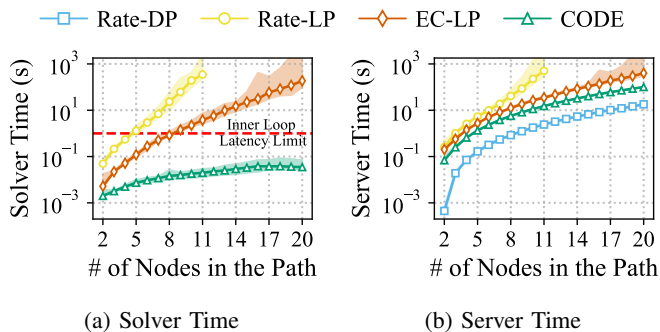


Fig. 9: Running time vs. number of physical links

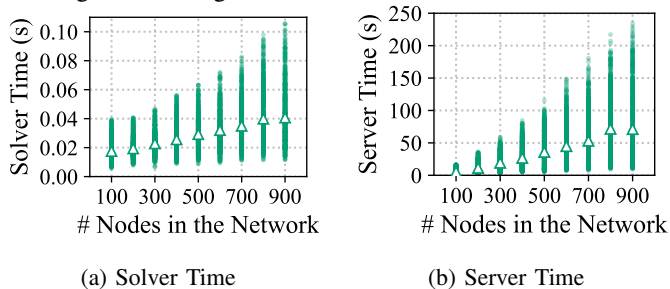


Fig. 10: Running time vs. number of nodes in the QN.

onds to 10^2 seconds. Because the Outer Loop is responsible for longer-term, structural network decisions, it is designed to operate on a timescale greater than 1 second. Even at the maximum evaluated network size of 900 nodes, the median Server Time remains computationally reasonable for background processing (peaking around $< 10^2$ seconds). This demonstrates that while the state space naturally grows with the underlying infrastructure, CODE’s dynamic programming-based generation efficiently manages this expansion.

The operational viability of CODE is validated by its exceptional Solver Time performance in fig. 10a. Despite the network scaling up to 900 nodes, the LP execution time remains bounded below 0.10 seconds. In fact, the vast majority of instances, including the medians, cluster heavily between 10^{-3} and $8 \cdot 10^{-2}$ seconds. This remarkable stability highlights the core architectural advantage of CODE: by absorbing the complexity of state space exploration into the non-RT Outer Loop, the Inner Loop is shielded from the combinatorial explosion typically associated with large network topologies.

IX. CONCLUSIONS

In this work, we addressed the multifaceted challenges of the entanglement distribution problem by introducing four pivotal advances for the practical deployment of Quantum Networks (QNs). First, we derived the Ensemble Capacity metric to shift the optimization objective toward maximizing the secure transmission of classical private information. Second, we presented a generalized mathematical formulation that lifts legacy structural restrictions, enabling the arbitrary sequencing of entanglement swapping and purification. Third, we proposed a Dynamic Programming (DP)-based algorithm that circumvents artificial fidelity quantization, preserving exact continuous quantum states while efficiently pruning the combinatorial space. Finally, we encapsulated these innovations into CODE, a two-tiered orchestration framework enabling

near-real-time network adaptivity. Evaluated under realistic physical hardware models, our methodology achieves superior private classical information capacity and drastically reduced computational overhead. By strictly satisfying dynamic latency constraints, this approach marks a substantial step toward the practical implementation of QNs.

REFERENCES

- [1] M. Travagnin, A. Lewis *et al.*, “Quantum key distribution in-field implementations,” *Publications Office of the European Union*, 2019.
- [2] M. Hillery, V. Bužek, and A. Berthiaume, “Quantum secret sharing,” *Physical Review A*, vol. 59, no. 3, p. 1829, 1999.
- [3] Z. Qi, Y. Li, Y. Huang, J. Feng, Y. Zheng, and X. Chen, “A 15-user quantum secure direct communication network,” *Light: Science & Applications*, vol. 10, no. 1, p. 183, 2021.
- [4] S. Pirandola, R. Laurenza, C. Ottaviani, and L. Banchi, “Fundamental limits of repeaterless quantum communications,” *Nature communications*, vol. 8, no. 1, p. 15043, 2017.
- [5] M. Caleffi, A. S. Cacciapuoti, and G. Bianchi, “Quantum internet: From communication to distributed computing!” in *Proceedings of the 5th ACM international conference on nanoscale computing and communication*, 2018, pp. 1–4.
- [6] W. Dür, H.-J. Briegel, J. I. Cirac, and P. Zoller, “Quantum repeaters based on entanglement purification,” *Physical Review A*, vol. 59, no. 1, p. 169, 1999.
- [7] W. J. Munro, K. Azuma, K. Tamaki, and K. Nemoto, “Inside quantum repeaters,” *IEEE Journal of Selected topics in quantum electronics*, vol. 21, no. 3, pp. 78–90, 2015.
- [8] J.-W. Pan, D. Bouwmeester, H. Weinfurter, and A. Zeilinger, “Experimental entanglement swapping: entangling photons that never interacted,” *Physical review letters*, vol. 80, no. 18, p. 3891, 1998.
- [9] J.-W. Pan, C. Simon, Č. Brukner, and A. Zeilinger, “Entanglement purification for quantum communication,” *Nature*, vol. 410, no. 6832, pp. 1067–1070, 2001.
- [10] M. Victora, S. Tserkis, S. Krastanov, A. S. de la Cerda, S. Willis, and P. Narang, “Entanglement purification on quantum networks,” *Physical Review Research*, vol. 5, no. 3, p. 033171, 2023.
- [11] H. Gu, R. Yu, Z. Li, X. Wang, and F. Zhou, “Esdi: Entanglement scheduling and distribution in the quantum internet,” in *2023 32nd International Conference on Computer Communications and Networks (ICCCN)*. IEEE, 2023, pp. 1–10.
- [12] H. Gu, Z. Li, R. Yu, X. Wang, F. Zhou, J. Liu, and G. Xue, “Fendi: Toward high-fidelity entanglement distribution in the quantum internet,” *IEEE/ACM Transactions on Networking*, vol. 32, no. 6, pp. 5033–5048, 2024.
- [13] I. Devetak, “The private classical capacity and quantum capacity of a quantum channel,” *IEEE Transactions on Information Theory*, vol. 51, no. 1, pp. 44–55, 2005.
- [14] X. Fan, Y. Yang, H. Gupta, and C. Ramakrishnan, “Distribution and purification of entanglement states in quantum networks,” in *2025 International Conference on Quantum Communications, Networking, and Computing (QCNC)*. IEEE, 2025, pp. 74–82.
- [15] M. Caleffi, “Optimal routing for quantum networks,” *Ieee Access*, vol. 5, pp. 22 299–22 312, 2017.
- [16] M. Pant, H. Krovi, D. Towsley, L. Tassiulas, L. Jiang, P. Basu, D. Englund, and S. Guha, “Routing entanglement in the quantum internet,” *npj Quantum Information*, vol. 5, no. 1, p. 25, 2019.
- [17] E. Grant, “On the stochastic analysis of a quantum entanglement distribution switch,” *Science China Physics, Mechanics & Astronomy*, vol. 66, no. 5, p. 250301, 2023.
- [18] H. Gu, Z. Li, X. Wang, D. Yang, G. Xue, and R. Yu, “Cost-aware high-fidelity entanglement distribution and purification in the quantum internet,” *IEEE Transactions on Networking*, 2025.
- [19] X. Sun, T. Hu, H. Chen, T. Zhu, and X. Jiang, “High-fidelity entanglement distribution method for quantum communication network,” in *2024 43rd Chinese Control Conference (CCC)*. IEEE, 2024, pp. 6771–6776.
- [20] C. Li, T. Li, Y.-X. Liu, and P. Cappellaro, “Effective routing design for remote entanglement generation on quantum networks,” *npj Quantum Information*, vol. 7, no. 1, p. 10, 2021.
- [21] Y. Zhao, G. Zhao, and C. Qiao, “E2e fidelity aware routing and purification for throughput maximization in quantum networks,” in *IEEE INFOCOM 2022-IEEE Conference on Computer Communications*. IEEE, 2022, pp. 480–489.

- [22] L. Chen and Z. Jia, "On optimum entanglement purification scheduling in quantum networks," *IEEE Journal on Selected Areas in Communications*, vol. 42, no. 7, pp. 1779–1792, 2024.
- [23] K. Chakraborty, F. Rozpedek, A. Dahlberg, and S. Wehner, "Distributed routing in a quantum internet," *arXiv preprint arXiv:1907.11630*, 2019.
- [24] K. Chakraborty, D. Elkouss, B. Rijsman, and S. Wehner, "Entanglement distribution in a quantum network: A multicommodity flow-based approach," *IEEE Transactions on Quantum Engineering*, vol. 1, pp. 1–21, 2020.
- [25] J. Li, M. Wang, K. Xue, R. Li, N. Yu, Q. Sun, and J. Lu, "Fidelity-guaranteed entanglement routing in quantum networks," *IEEE Transactions on Communications*, vol. 70, no. 10, pp. 6748–6763, 2022.
- [26] S. Bratzik, S. Abruzzo, H. Kampermann, and D. Bruß, "Quantum repeaters and quantum key distribution: The impact of entanglement distillation on the secret key rate," *Physical Review A Atomic, Molecular, and Optical Physics*, vol. 87, no. 6, p. 062335, 2013.
- [27] S. Pirandola, "End-to-end capacities of a quantum communication network," *Communications Physics*, vol. 2, no. 1, p. 51, 2019.
- [28] A. Einstein, B. Podolsky, and N. Rosen, "Can quantum-mechanical description of physical reality be considered complete?" *Physical review*, vol. 47, no. 10, p. 777, 1935.
- [29] D. Huber, M. Reindl, Y. Huo, H. Huang, J. S. Wildmann, O. G. Schmidt, A. Rastelli, and R. Trotta, "Highly indistinguishable and strongly entangled photons from symmetric gas quantum dots," *Nature communications*, vol. 8, no. 1, p. 15506, 2017.
- [30] I. Aharonovich, D. Englund, and M. Toth, "Solid-state single-photon emitters," *Nature photonics*, vol. 10, no. 10, pp. 631–641, 2016.
- [31] L.-M. Duan, M. D. Lukin, J. I. Cirac, and P. Zoller, "Long-distance quantum communication with atomic ensembles and linear optics," *Nature*, vol. 414, no. 6862, pp. 413–418, 2001.
- [32] B. J. Smith, P. Mahou, O. Cohen, J. Lundeen, and I. Walmsley, "Photon pair generation in birefringent optical fibers," *Optics express*, vol. 17, no. 26, pp. 23 589–23 602, 2009.
- [33] C. H. Bennett, G. Brassard, C. Crépeau, R. Jozsa, A. Peres, and W. K. Wootters, "Teleporting an unknown quantum state via dual classical and einstein-podolsky-rosen channels," *Physical review letters*, vol. 70, no. 13, p. 1895, 1993.
- [34] C. H. Bennett, D. P. DiVincenzo, J. A. Smolin, and W. K. Wootters, "Mixed-state entanglement and quantum error correction," *Physical Review A*, vol. 54, no. 5, p. 3824, 1996.
- [35] W. Dür and H. J. Briegel, "Entanglement purification and quantum error correction," *Reports on Progress in Physics*, vol. 70, no. 8, pp. 1381–1424, 2007.
- [36] Q. Zhang, N. Di Cicco, M. Ibrahim, R. C. Almeida, A. Gatto, R. Boutaba, and M. Tornatore, "Link configuration for fidelity-constrained entanglement routing in quantum networks," in *IEEE INFOCOM 2025-IEEE Conference on Computer Communications*. IEEE, 2025, pp. 1–10.
- [37] S. Pouryousef, N. K. Panigrahy, and D. Towsley, "A quantum overlay network for efficient entanglement distribution," in *IEEE INFOCOM 2023-IEEE Conference on Computer Communications*. IEEE, 2023, pp. 1–10.
- [38] M. F. Askarani, K. Chakraborty, and G. Castro do Amaral, "Entanglement distribution in multi-platform buffered-router-assisted frequency-multiplexed automated repeater chains," *New Journal of Physics*, vol. 23, no. 6, p. 063078, 2021.
- [39] G. Bowen and S. Bose, "Teleportation as a depolarizing quantum channel, relative entropy, and classical capacity," *Physical Review Letters*, vol. 87, no. 26, p. 267901, 2001.
- [40] C. H. Bennett, G. Brassard, and N. D. Mermin, "Quantum cryptography without bells theorem," *Physical review letters*, vol. 68, no. 5, p. 557, 1992.
- [41] W. Kozłowski, A. Dahlberg, and S. Wehner, "Designing a quantum network protocol," in *Proceedings of the 16th international conference on emerging networking experiments and technologies*, 2020, pp. 1–16.
- [42] H. Jacinto, É. Gouzien, and N. Sangouard, "Network requirements for distributed quantum computation," *Physical Review Research*, vol. 8, no. 1, p. 013205, 2026.
- [43] D. Pérez Castro, A. Fernández Vilas, M. Fernández Veiga, M. Blanco Rodríguez, and R. P. Díaz Redondo, "Simulation of fidelity in entanglement-based networks with repeater chains," *Applied Sciences*, vol. 14, no. 23, p. 11270, 2024.
- [44] P. Zhang and G. Chartrand, *Introduction to graph theory*. Tata McGraw-Hill New York, 2006, vol. 2, no. 2.1.
- [45] S. Roman *et al.*, *An introduction to Catalan numbers*. Springer, 2015.
- [46] D. Bertsekas, *Reinforcement learning and optimal control*. Athena Scientific, 2019, vol. 1.
- [47] R. J. Vanderbei, "Linear programming: foundations and extensions," *Journal of the Operational Research Society*, vol. 49, no. 1, pp. 94–94, 1998.
- [48] T. Coopmans, R. Knegjens, A. Dahlberg, D. Maier, L. Nijsten, J. de Oliveira Filho, M. Papendrecht, J. Rabbie, F. Rozpedek, M. Skrzypczyk *et al.*, "Netsquid, a network simulator for quantum information using discrete events," *Communications Physics*, vol. 4, no. 1, p. 164, 2021.
- [49] A. Zang, A. Kolar, J. Chung, M. Suchara, T. Zhong, and R. Kettimuthu, "Simulation of entanglement generation between absorptive quantum memories," in *2022 IEEE International Conference on Quantum Computing and Engineering (QCE)*. IEEE, 2022, pp. 617–623.
- [50] H. Hübel, M. R. Vanner, T. Lederer, B. Blauensteiner, T. Lorünser, A. Poppe, and A. Zeilinger, "High-fidelity transmission of polarization encoded qubits from an entangled source over 100 km of fiber," *Optics Express*, vol. 15, no. 12, pp. 7853–7862, 2007.
- [51] A. Labay Mora, F. Ferreira da Silva, and S. Wehner, "Reducing hardware requirements for entanglement distribution via joint hardware-protocol optimization," *Quantum Science and Technology*, vol. 9, no. 4, p. 045001, 2024.
- [52] R. Barends, J. Kelly, A. Megrant, A. Veitia, D. Sank, E. Jeffrey, T. C. White, J. Mutus, A. G. Fowler, B. Campbell *et al.*, "Superconducting quantum circuits at the surface code threshold for fault tolerance," *Nature*, vol. 508, no. 7497, pp. 500–503, 2014.
- [53] F. Steinlechner, P. Trojek, M. Jofre, H. Weier, D. Perez, T. Jennewein, R. Ursin, J. Rarity, M. W. Mitchell, J. P. Torres *et al.*, "A high-brightness source of polarization-entangled photons optimized for applications in free space," *Optics express*, vol. 20, no. 9, pp. 9640–9649, 2012.
- [54] S. Magnitskiy, D. Frolovstev, V. Firsov, P. Gostev, I. Protchenko, and M. Saygin, "A spdc-based source of entangled photons and its characterization," *Journal of Russian Laser Research*, vol. 36, no. 6, pp. 618–629, 2015.
- [55] C. W. Helstrom, "Quantum detection and estimation theory," *Journal of statistical physics*, vol. 1, no. 2, pp. 231–252, 1969.
- [56] J. P. Dehollain, J. T. Muhonen, R. Blume-Kohout, K. M. Rudinger, J. K. Gamble, E. Nielsen, A. Laucht, S. Simmons, R. Kalra, A. S. Dzurak *et al.*, "Optimization of a solid-state electron spin qubit using gate set tomography," *New Journal of Physics*, vol. 18, no. 10, p. 103018, 2016.
- [57] D. A. Rower, L. Ding, H. Zhang, M. Hays, J. An, P. M. Harrington, I. T. Rosen, J. M. Gertler, T. M. Hazard, B. M. Niedzielski *et al.*, "Suppressing counter-rotating errors for fast single-qubit gates with fluxonium," *PRX Quantum*, vol. 5, no. 4, p. 040342, 2024.
- [58] M. AbuGhanem and H. Eleuch, "Full quantum tomography study of googles sycamore gate on ibms quantum computers," *EPJ Quantum Technology*, vol. 11, no. 1, p. 36, 2024.
- [59] P. Wang, C.-Y. Luan, M. Qiao, M. Um, J. Zhang, Y. Wang, X. Yuan, M. Gu, J. Zhang, and K. Kim, "Single ion qubit with estimated coherence time exceeding one hour," *Nature communications*, vol. 12, no. 1, p. 233, 2021.
- [60] M. H. Abobeih, J. Cramer, M. A. Bakker, N. Kalb, M. Markham, D. J. Twitchen, and T. H. Taminiau, "One-second coherence for a single electron spin coupled to a multi-qubit nuclear-spin environment," *Nature communications*, vol. 9, no. 1, p. 2552, 2018.
- [61] C. E. Bradley, J. Randall, M. H. Abobeih, R. C. Berrevoets, M. J. Degen, M. A. Bakker, M. Markham, D. J. Twitchen, and T. H. Taminiau, "A ten-qubit solid-state spin register with quantum memory up to one minute," *Physical Review X*, vol. 9, no. 3, p. 031045, 2019.
- [62] D. Deutsch, A. Ekert, R. Jozsa, C. Macchiavello, S. Popescu, and A. Sanpera, "Quantum privacy amplification and the security of quantum cryptography over noisy channels," *Physical review letters*, vol. 77, no. 13, p. 2818, 1996.
- [63] F. Rozpedek, T. Schiet, L. P. Thinh, D. Elkouss, A. C. Doherty, and S. Wehner, "Optimizing practical entanglement distillation," *Physical Review A*, vol. 97, no. 6, p. 062333, 2018.
- [64] P. Jurkiewicz, "Topohub: A repository of reference gabriel graph and real-world topologies for networking research," *SoftwareX*, vol. 24, p. 101540, 2023.
- [65] E. K. Cetinkaya, M. J. Alenazi, Y. Cheng, A. M. Peck, and J. P. Sterbenz, "On the fitness of geographic graph generators for modelling physical level topologies," in *2013 5th International Congress on Ultra Modern Telecommunications and Control Systems and Workshops (ICUMT)*. IEEE, 2013, pp. 38–45.
- [66] S. Knight, H. X. Nguyen, N. Falkner, R. Bowden, and M. Roughan, "The internet topology zoo," *IEEE Journal on Selected Areas in Communications*, vol. 29, no. 9, pp. 1765–1775, 2011.